

# Numerically Informed Convolutional Operator Network with Subproblem Decomposition for Poisson Equations

Kyoungjin Jung,\* Jae Yong Lee<sup>†</sup> and Dongwook Shin<sup>‡</sup>

## Abstract

Neural operators have shown remarkable performance in approximating solutions of partial differential equations. However, their convergence behavior under grid refinement is still not well understood from the viewpoint of numerical analysis. In this work, we propose a numerically informed convolutional operator network, called NICON, that explicitly couples classical finite difference and finite element methods with operator learning through residual-based training loss functions. We introduce two types of networks, FD-CON and FE-CON, which use residual-based loss functions derived from the corresponding numerical methods. We derive error estimates for FD-CON and FE-CON using finite difference and finite element analysis. These estimates show a direct relation between the convergence behavior and the decay rate of the training loss. From these analyses, we establish training strategies that guarantee optimal convergence rates under grid refinement. Several numerical experiments are presented to validate the theoretical results and show performance on fine grids.

## 1 Introduction

Solving partial differential equations (PDEs) is a fundamental task in computational science, with applications ranging from physics and engineering to climate modeling and biology. Classical numerical solvers, such as finite difference method (FDM) and finite element method (FEM), provide accurate solutions but often require significant computational cost when solving parameterized families of PDEs across multiple input configurations. This limitation becomes particularly severe on fine grids, where repeated solutions of large linear systems or the storage of dense inverse operators are prohibitive.

Operator learning [20, 13] has gained attention as an alternative approach that aims to directly learn mappings from input functions, such as source terms and boundary data, to PDE solutions. Despite this progress, existing neural operators exhibit several critical limitations. First, most operators are trained in a supervised setting and rely on large datasets of input–output pairs, which are expensive to generate using classical solvers [14]. This dependence severely limits scalability, especially in applications where ground-truth solutions are unavailable or prohibitive expensive to compute. Second, generalization to diverse boundary conditions remains a significant challenge [26]. Many existing models are designed under fixed or simplified boundary types—such as periodic or purely Dirichlet boundary conditions—and often fail to adapt to new configurations, particularly when Neumann or mixed boundary conditions are introduced. Third, current approaches typically treat PDEs as black-box mappings without exploiting known mathematical structures such as linearity or decomposability. As a result, models may overfit specific input patterns and lack the interpretability and modularity needed for more complex scientific applications.

---

\*Department of Mathematics, Ajou University, Suwon, Republic of Korea. Email: [fned49@ajou.ac.kr](mailto:fned49@ajou.ac.kr)

<sup>†</sup>Department of AI, Chung-Ang University, Seoul, Republic of Korea. Email: [jaeyong@cau.ac.kr](mailto:jaeyong@cau.ac.kr)

<sup>‡</sup>Department of Mathematics, Ajou University, Suwon, Republic of Korea. Email: [dws@ajou.ac.kr](mailto:dws@ajou.ac.kr)

Recently, convolution-based neural operator architectures have been proposed to improve the scalability and expressivity of operator learning models [30, 31]. In particular, the convolutional neural operator [23] introduces structure-preserving modifications to Convolutional Neural Networks (CNNs) to enforce continuous-discrete equivalence and reduce aliasing errors. This approach provides a principled operator-level adaptation of U-Net architectures [24]. This line of work addresses important representation-theoretic challenges in operator learning, especially those related to discretization dependence and aliasing effects in convolutional architectures. However, these advances primarily focus on how operators are represented and learned across resolutions, rather than on the incorporation of physical laws and numerical discretizations into the training process. In particular, the governing PDE structure typically enters such models only implicitly, and the training procedure remains largely decoupled from classical numerical schemes. As a result, these models do not explicitly exploit the consistency, locality, and stability properties inherent in numerical methods. In many scientific and engineering applications, the governing equations are explicitly known, while the paired solution data may be expensive or impractical to obtain. This observation motivates operator learning frameworks that directly integrate numerical discretizations and physics-based constraints into the learning process. Such frameworks enable training driven by the PDE itself rather than by precomputed solution pairs.

These considerations motivate the development of operator learning frameworks that explicitly integrate physical laws and numerical discretizations into the learning process. In this work, we propose an operator learning framework, **Numerically Informed Convolutional Operator Network (NICON)**, which combines physics-informed convolutional networks with classical numerical schemes. Our method is compatible with both finite difference and finite element methods and is realized through two approaches: the **Finite Difference Convolutional Operator Network (FD-CON)** and the **Finite Element Convolutional Operator Network (FE-CON)**. These approaches share a common architecture but differ in the construction of their loss functions, which are based on residuals derived from FDM and FEM, respectively. To further enhance training efficiency and generalization, we introduce a decomposition strategy that splits the original Poisson problem into two simpler subproblems by exploiting the linearity of the equation. Each subproblem is modeled independently, and its predictions are combined linearly to recover the approximate solution. This decomposition allows each model to focus on a smaller and more structured task, which improves prediction accuracy and significantly reduces the number of required training samples.

The main contributions of this paper are as follows:

- **Mixed boundary conditions and fully varying data.** We consider the Poisson equation with mixed (Dirichlet–Neumann) boundary conditions and allow all three components—the source term, Dirichlet and Neumann boundary conditions—to vary freely. This setting differs from prior works, which typically vary only one component while keeping the others fixed.
- **Domain-to-image mapping.** We map the computational domain onto an image so that no spatial distortion occurs even for complex geometries. This mapping enables effective CNN-based operator learning.
- **Error analysis and training strategy.** We derive error estimates based on finite difference and finite element analyses, and propose a training strategy to achieve the optimal convergence rate with respect to the mesh size for a fixed number of training samples.
- **Experiments on fine grids.** Our models train reliably on fine grids and produce accurate solutions. We also present an experiment that quantifies the relationship between generalization error and the number of training samples used during training.
- **Decomposition strategy for efficiency and accuracy.** We decompose the model problem into two subproblems and train separate operator models. This strategy improves training efficiency and inference accuracy, particularly when only a limited number of training samples are available.

The remainder of this paper is organized as follows. The next section provides a brief introduction to classical numerical schemes and related works. Section 3 describes the discretization and numerical schemes for both finite difference and finite element convolutional operator networks. The error analysis in the  $H^1$ -seminorm is also presented. Section 4 provides experimental results demonstrating the accuracy, training efficiency, and scalability of our approach. We conclude in Section 5 with a discussion of future directions.

## 2 Preliminaries

In this section, we review the background necessary for this work. We first summarize classical finite difference and finite element methods. We then review various machine-learning-based approaches for learning PDE operators. Finally, we discuss inference efficiency from an operator perspective by interpreting the computation of the inverse matrix of the finite element system as training and its application as inference. This perspective enables a unified comparison between classical solvers and machine-learning-based methods and motivates the proposed approach.

### 2.1 Classical Numerical Discretizations

Let us consider the following Poisson's equation with mixed boundary conditions:

$$-\Delta u = f \quad \text{in } \Omega, \quad (1a)$$

$$u = g_D \quad \text{on } \partial\Omega_D, \quad (1b)$$

$$\nabla u \cdot \mathbf{n} = g_N \quad \text{on } \partial\Omega_N, \quad (1c)$$

where  $\Omega \subset \mathbb{R}^d$  ( $d = 1, 2, 3$ ) is a bounded Lipschitz domain with polygonal boundary  $\partial\Omega$ ,  $\partial\Omega_D$  is the Dirichlet boundary, and  $\partial\Omega_N$  is the Neumann boundary. Here,  $\partial\Omega_D$  is a closed subset of  $\partial\Omega$  with positive length and  $\partial\Omega_N = \partial\Omega \setminus \partial\Omega_D$ . For simplicity, we focus on the two-dimensional case ( $d = 2$ ) throughout the remainder of this paper.

We first briefly review a standard finite difference discretization on a uniform grid. Without loss of generality, we consider a uniform grid with  $x_i < x_{i+1}$ ,  $y_j < y_{j+1}$ , and  $h := x_{i+1} - x_i = y_{j+1} - y_j$  for  $i = 1, 2, \dots, N_x$  and  $j = 1, 2, \dots, N_y$ . Here, we define a single global index for each node by using a row-major ordering,  $k = (N_x - 1)(j - 1) + i$ , and denote the corresponding node by  $\eta_k = (x_i, y_j)$ . Let  $u_{i,j} = u(x_i, y_j)$ . Then, finite difference approximations to the Laplacian  $\Delta$  are given by:

$$\text{5-point stencil: } \Delta_h u = \frac{u_{i-1,j} + u_{i+1,j} + u_{i,j-1} + u_{i,j+1} - 4u_{i,j}}{h^2}, \quad (2)$$

$$\begin{aligned} \text{9-point stencil: } \Delta_h u = & \frac{u_{i-1,j-1} + u_{i+1,j-1} + u_{i-1,j+1} + u_{i+1,j+1}}{6h^2} - \frac{20u_{i,j}}{6h^2} \\ & + \frac{4u_{i,j-1} + 4u_{i-1,j} + 4u_{i+1,j} + 4u_{i,j+1}}{6h^2}. \end{aligned} \quad (3)$$

For first-order partial derivatives on the Neumann boundary, we use the following forward or backward differences depending on the boundary location:

$$\partial_x^+ u(x_i, y_j) = \frac{u_{i+1,j} - u_{i,j}}{h} \quad \text{or} \quad \partial_x^- u(x_i, y_j) = \frac{u_{i,j} - u_{i-1,j}}{h}, \quad (4a)$$

$$\partial_y^+ u(x_i, y_j) = \frac{u_{i,j+1} - u_{i,j}}{h} \quad \text{or} \quad \partial_y^- u(x_i, y_j) = \frac{u_{i,j} - u_{i,j-1}}{h}. \quad (4b)$$

For a boundary node  $(x_i, y_j)$ , we use  $\partial_x^+ u$  if the interior neighbor in the x-direction is at index  $i + 1$ ; we use  $\partial_x^- u$  if the interior neighbor is at index  $i - 1$ . The same rule applies in the  $y$ -direction. Then,

with  $\nabla_h u = (\partial_x^\pm u, \partial_y^\pm u)$ , the finite difference method is to find  $u_h$  such that

$$-\Delta_h u_h(x_i, y_j) = f(x_i, y_j) \quad \forall (x_i, y_j) \in \Omega \setminus \partial\Omega, \quad (5a)$$

$$u_h(x_i, y_j) = g_D(x_i, y_j) \quad \forall (x_i, y_j) \in \partial\Omega_D, \quad (5b)$$

$$\nabla_h u_h(x_i, y_j) \cdot \mathbf{n} = g_N(x_i, y_j) \quad \forall (x_i, y_j) \in \partial\Omega_N. \quad (5c)$$

We next summarize the finite element formulation with mixed boundary conditions. Let us denote an extension of  $g_D$  by  $u_D$ , which is a function defined on the whole domain and  $u_D = g_D$  on  $\partial\Omega_D$ . If  $f \in L^2(\Omega)$ ,  $u_D \in H^1(\Omega)$ , and  $g_N \in L^2(\partial\Omega_N)$ , there exists a weak solution  $u \in H^1(\Omega)$  by the Lax–Milgram lemma. In order to deal with the inhomogeneous Dirichlet conditions (1b), we consider the decomposition  $u = w + u_D$  for  $w \in H_D^1(\Omega)$ , where  $H_D^1(\Omega) := \{v \in H^1(\Omega) \mid v = 0 \text{ on } \partial\Omega_D\}$ . The weak formulation reads: find  $w \in H_D^1(\Omega)$  such that

$$\int_{\Omega} \nabla w \cdot \nabla v \, dx = \int_{\Omega} f v \, dx + \int_{\partial\Omega_N} g_N v \, ds - \int_{\Omega} \nabla u_D \cdot \nabla v \, dx, \quad (6)$$

for all  $v \in H_D^1(\Omega)$ .

For the implementation, we consider finite element spaces  $S$  and  $S_D \subset S \cap H_D^1(\Omega)$  which are finite-dimensional subspaces of  $H^1(\Omega)$  and  $H_D^1(\Omega)$ , respectively. For a given  $U_D \in S$  which approximates  $u_D$  on  $\partial\Omega_D$ , the discretized problem reads: Find  $W \in S_D$  such that

$$\int_{\Omega} \nabla W \cdot \nabla V \, dx = \int_{\Omega} f V \, dx + \int_{\partial\Omega_N} g_N V \, ds - \int_{\Omega} \nabla U_D \cdot \nabla V \, dx, \quad (7)$$

for all  $V \in S_D$ . Let  $\{\eta_i\}_{i=1}^N$  denote the node points on a given mesh of  $\Omega$  and  $\{\psi_i\}_{i=1}^N$  denote the basis of  $S$  satisfying  $\psi_i(\eta_j) = \delta_{ij}$ . Let  $\{\psi_{i_k}\}_{k=1}^M$  denote the basis of  $S_D$ , where  $I = \{i_1, \dots, i_M\} \subseteq \{1, \dots, N\}$  is an index set of cardinality  $M \leq N - 2$ . Then, (7) is equivalent to

$$\int_{\Omega} \nabla W \cdot \nabla \psi_j \, dx = \int_{\Omega} f \psi_j \, dx + \int_{\partial\Omega_N} g_N \psi_j \, ds - \int_{\Omega} \nabla U_D \cdot \nabla \psi_j \, dx, \quad (8)$$

for all  $j \in I$ . Furthermore, let

$$W = \sum_{k \in I} w_k \psi_k \quad \text{and} \quad U_D = \sum_{i=1}^N U_i \psi_i. \quad (9)$$

For simplicity, we set  $U_i = 0$  if  $\eta_i \notin \partial\Omega_D$  and define  $U_D$  as the nodal interpolant of  $g_D$  on  $\partial\Omega_D$ , i.e.,  $U_i = g_D(\eta_i)$  if  $\eta_i \in \partial\Omega_D$ . Then, (7) yields the following linear system of equations

$$\mathbf{A}\mathbf{w} = \mathbf{b} \quad (10)$$

where

$$A_{jk} = \int_{\Omega} \nabla \psi_j \cdot \nabla \psi_k \, dx, \quad (11a)$$

$$b_j = \int_{\Omega} f \psi_j \, dx + \int_{\partial\Omega_N} g_N \psi_j \, ds - \sum_{k=1}^N U_k \int_{\Omega} \nabla \psi_j \cdot \nabla \psi_k \, dx. \quad (11b)$$

Here, the matrix  $\mathbf{A} = (A_{jk})_{j,k \in I} \in \mathbb{R}^{M \times M}$  is called the global stiffness matrix and the right-hand side  $\mathbf{b} = (b_j)_{j \in I} \in \mathbb{R}^M$  is called the load vector. The global stiffness matrix is sparse, symmetric and positive definite, so (10) has exactly one solution  $\mathbf{w} \in \mathbb{R}^M$  which determines the finite element solution

$$U = W + U_D = \sum_{k \in I} w_k \psi_k + \sum_{i=1}^N U_i \psi_i. \quad (12)$$

**Remark 2.1.** *In the implementation, defining both  $W$  and  $U_D$  is a waste of memory. Since by definition  $W = 0$  if  $\eta_i \in \partial\Omega_D$  and  $U_D = 0$  if  $\eta_i \notin \partial\Omega_D$ , they can be represented by a single vector. Specifically, we first set  $U = \sum_{i=1}^N u_i \psi_i$ , where  $u_i = 0$  if  $\eta_i \notin \partial\Omega_D$  and  $u_i = g_D(\eta_i)$  if  $\eta_i \in \partial\Omega_D$ . After computing (11b), the solution of the linear system (10) is stored in the entries corresponding to  $u_i$  where  $\eta_i \notin \partial\Omega_D$ , i.e.,  $U_i = w_i$  if  $\eta_i \notin \partial\Omega_D$ .*

## 2.2 Machine-Learning Approaches: Related Works

Recent advances in physics-informed machine learning [12] have led to a growing interest in solving PDEs using neural networks. Notable examples include physics-informed neural networks (PINNs) [22], which embed physical laws into the loss function to guide physical dynamics. Building on this idea, an increasing body of work has focused on learning mappings between infinite-dimensional function spaces—known as neural operators. Early works such as convolutional neural networks (CNNs) explored function-to-function learning via convolutional architectures, showing promising results across various application domains [31]. Subsequent advances introduced theoretical guarantees such as universal approximation theorems, motivating the development of the Deep Operator Network (DeepONet) [19] and its many variants [20, 15]. In parallel, the Fourier Neural Operator (FNO) [17] proposed a spectral kernel-learning approach in place of classical linear layers, enabling efficient approximation of PDE solution operators in high-dimensional settings. These foundational models have since been extended with ideas from meta-learning [6, 7], graph neural networks [3, 2, 5], and transformers [10, 27, 4], yielding new classes of neural operators tailored to complex, structured data.

CNN-based models have also adopted U-Net architectures to enable robust and accurate operator learning in image-based domains, along with theoretical results on their approximation capacity [23]. In addition, hybrid approaches that integrate classical numerical solvers, such as FDM [1], with deep learning have been explored to improve data efficiency and utilize domain-specific inductive biases. Despite these successes, most neural operator frameworks are trained in a supervised manner and require large collections of paired input–output data, which are often generated via computationally expensive numerical solvers. This reliance on labeled data presents a critical bottleneck, particularly for large-scale or parametric PDE [8].

To mitigate this limitation, data-free or physics-informed neural operators have recently gained attention [9]. For example, Zhu et al. [31] proposed a CNN-based method that incorporates finite difference discretizations and learns operators directly from PDE residuals. The Physics-Informed DeepONet (PI-DeepONet) [29] extended DeepONet to an unsupervised setting by minimizing residuals instead of relying on labeled data. Similarly, the Physics-Informed Neural Operator (PINO) [18] introduced a loss formulation that enables FNO training with limited or no supervision. More recently, Finite Element Operator Network (FEONet) [16], proposed by Lee et al., leveraged a finite element formulation to learn solution operators without labeled data, achieving strong performance across a variety of PDE benchmarks.

In parallel, several studies have investigated mechanisms to better enforce or satisfy boundary conditions within neural operator frameworks [26, 25, 16]. While progress has been made in handling Dirichlet or periodic boundary conditions through network architectures and loss design, a general and scalable approach that can handle mixed or variable boundary conditions across resolutions remains underexplored. Our work addresses this gap by proposing a decomposition-based formulation that naturally accommodates diverse boundary configurations while maintaining fully data-free training.

## 2.3 Remarks on Inference Efficiency

In general, key evaluation metrics for neural operators include accuracy, generalization capability, and physical consistency. Training time is often treated as a secondary concern under the assumption that

Table 1: Comparison of memory usage (MB) and inference time (ms) with standard deviations (ms) between FEM and FE-CON.

Grid size	FEM		FE-CON(Ours)		Time ratio (FE-CON / FEM)
	Memory	Time	Memory	Time	
16×16	0.25	0.271 ± 0.008	0.11	0.531 ± 0.027	1.96
32×32	4.00	0.162 ± 0.005	1.84	0.672 ± 0.025	4.15
64×64	64.00	0.279 ± 0.008	29.60	1.434 ± 0.034	5.14
128×128	1024.00	1.710 ± 0.022	497.40	5.903 ± 0.071	3.45

sufficient computational resources are available, with emphasis placed on fast inference even when training is expensive. In the context of offline training, this assumption further implies that training time is not critical in practical applications. On the other hand, numerical models typically provide high accuracy, and many methods have been developed to preserve physical laws. However, these methods often suffer from high computational cost due to solving large linear systems. If training in numerical models is interpreted as the computation of a matrix inverse, then obtaining  $A^{-1}$  for the system (10) corresponds to the training phase. Once this is completed, inference reduces to a matrix-vector multiplication  $\mathbf{w} = A^{-1}\mathbf{b}$ , which can be performed efficiently.

Table 1 shows the memory usage and inference time for FEM and our proposed method (FE-CON). For both methods, only inference time is considered, excluding training time. In FEM, training is interpreted as computing  $A^{-1}$ , and the memory required to store  $A^{-1}$  is measured. The time required to compute  $\mathbf{b}$  in FEM is ignored, since both FEM and FE-CON use  $\mathbf{b}$  as input. Inference time for FEM refers to the time taken to compute  $A^{-1}\mathbf{b}$ , while for FE-CON, it is measured as the time elapsed from the input to the predicted solution. Since the inference time for a single input is very short, we report the average and standard deviation of the inference time measured over multiple independent inputs used in the numerical experiments. For a fair comparison, we used a single-precision data type for  $A^{-1}$ , and all computations were performed on a GPU using JAX. The inference time was measured after a warm-up phase to reduce JIT compilation overhead and ensure stable timing.

Although FEM requires approximately twice as much memory as our proposed model, it achieves faster inference. The higher memory usage in FEM indicates that the number of nonzero entries in  $A^{-1}$  exceeds the number of parameters in FE-CON. FEM performs a single matrix-vector multiplication  $A^{-1}\mathbf{b}$ , whereas our model relies on multiple convolutional layers and nonlinear activations. As a result, the inference time of FE-CON tends to be longer. However, as the grid becomes finer, the ratio of inference times between FEM and FE-CON decreases. Thus this suggests that FE-CON may achieve faster inference on sufficiently fine grids. Moreover, while FEM with a precomputed inverse can be competitive at moderate resolutions, its applicability is fundamentally limited by memory constraints on fine grids. In contrast, FE-CON avoids the explicit storage of dense inverse operators and provides a scalable alternative for high-resolution inference. This simple experiment shows that traditional numerical methods are not necessarily inferior to machine learning approaches in terms of inference speed for linear PDEs. To justify the use of machine learning approaches, one should consider finer grids or applications in which numerical solvers must compute solutions repeatedly, such as nonlinear PDEs or time-dependent problems.

### 3 Methodology

In this section, we present our framework, NICON, for training neural operators to solve the model problem (1). Our framework consists of two approaches: FD-CON and FE-CON, which apply physics-informed convolutional learning to discretized PDEs using finite difference and finite element

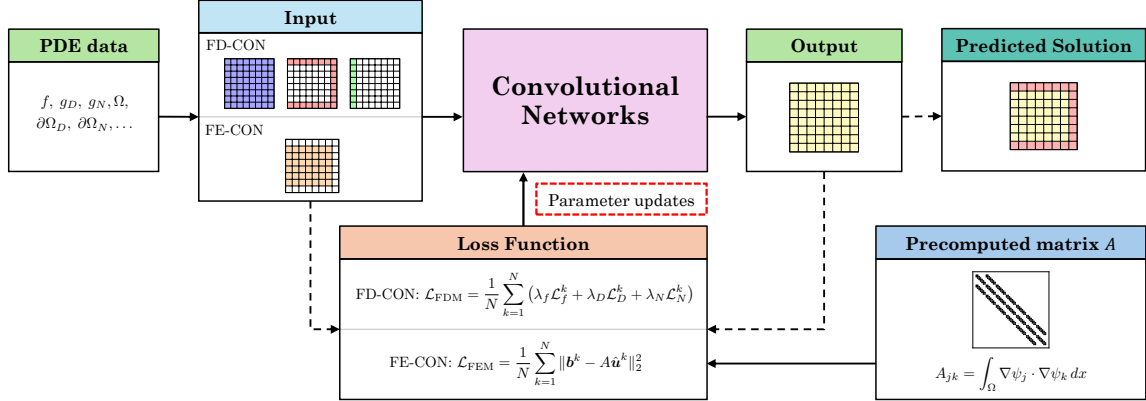


Figure 1: Schematic overview of the Numerically Informed Convolutional Operator Networks (NICON).

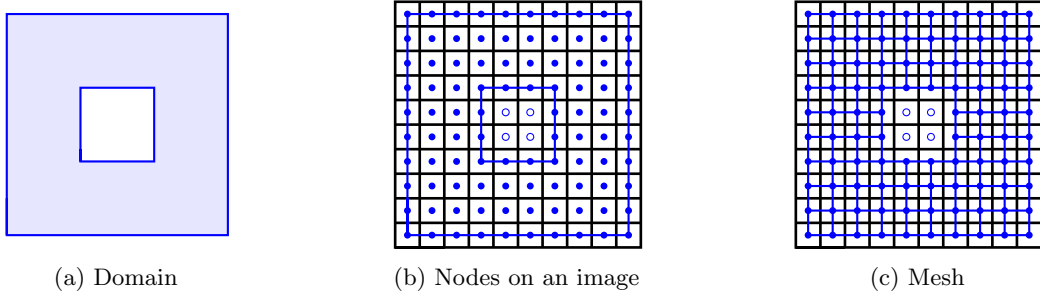


Figure 2: Illustration of the mesh generation process based on image-domain mapping.

formulations, respectively. A schematic overview of the NICON structure is given in Figure 1.

For simplicity, let us consider a square domain  $\Omega \subset \mathbb{R}^2$  and discretize the domain into a uniform square grid of size  $N \times N$ . In classical FDM or FEM, each node corresponds to a mesh vertex. In contrast, we adopt an image-based representation in which each node is represented as a pixel value on a 2D image grid. More precisely, we first specify the size of the input image and then map the computational domain onto this image. Then, blue nodes are placed at the pixels corresponding to the interior and boundary of the domain, and white nodes are placed at the pixels corresponding to regions outside the domain, as illustrated in Figure 2b. Finally, the mesh is constructed based on the positions of the blue nodes (see Figure 2c). We note that, although node alignment on a uniform grid simplifies the implementation of FD or FE schemes, such an alignment is not essential for the proposed approach. Node locations can be adjusted as long as the underlying geometric information is preserved. While this adjustment may introduce apparent distortion in the image representation, it does not affect training since the loss function is evaluated at the true spatial locations of the nodes. The solution can also be visualized accurately by reconstructing it using the physical coordinates. All nodes are numbered in the order of the image pixels, regardless of whether they are blue or white. The load vector  $\mathbf{b}$  in (11b) is defined on the full image grid, and its dimension thus matches the number of pixels in the input image. Only the entries associated with the blue nodes correspond to the degrees of freedom in the FE formulation and are evaluated through numerical integration using the true spatial coordinates, while the remaining entries are set to zero. Moreover, no physical or spatial distortion is introduced because all computations in the loss function are carried out using the true spatial coordinates of the nodes. A masking image can be used to enforce zero values at the corresponding pixels in the output as well.

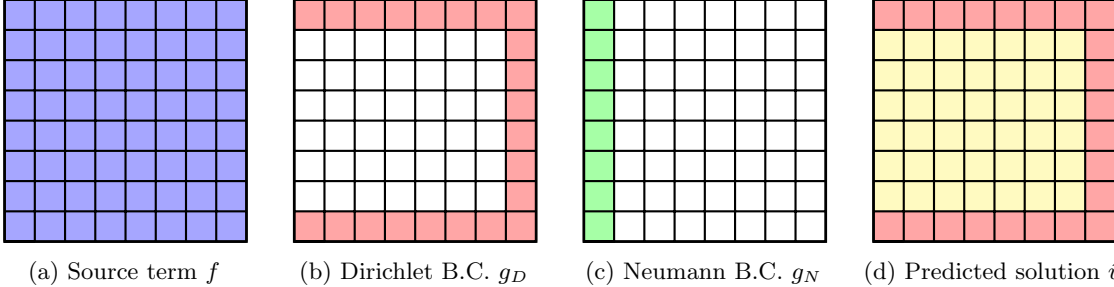


Figure 3: Input channels (a)–(c) and the predicted solution (d) for FD-CON. The source term  $f$  is provided over the entire domain, while the Dirichlet and Neumann boundary conditions are encoded as separate channels. The predicted solution is post-processed to enforce the Dirichlet boundary condition.

This approach allows us to embed the spatial structure of the PDE into a convolutional architecture, enabling the use of CNNs to approximate differential operators efficiently. Building on this formulation, we employ a fully convolutional neural network to approximate the solution operator; specific architectural choices are detailed in Section 4.1. The input to the network consists of one or more channels, depending on the problem type, and the output is a single-channel prediction of the solution  $u$ . The input and output of our CNN models share the same spatial resolution, as the architecture is fully convolutional and designed to preserve grid alignment throughout all layers.

To enable more efficient and flexible learning, we explicitly decompose the model problem (1) into the following subproblems:

### Subproblem 1

$$-\Delta u_1 = f \quad \text{in } \Omega \quad (13a)$$

$$u_1 = 0 \quad \text{on } \partial\Omega_D \quad (13b)$$

$$\nabla u_1 \cdot \mathbf{n} = g_N \quad \text{on } \partial\Omega_N \quad (13c)$$

### Subproblem 2

$$-\Delta u_2 = 0 \quad \text{in } \Omega \quad (14a)$$

$$u_2 = g_D \quad \text{on } \partial\Omega_D \quad (14b)$$

$$\nabla u_2 \cdot \mathbf{n} = 0 \quad \text{on } \partial\Omega_N \quad (14c)$$

By the superposition principle, the solution to the model problem can be written as

$$u = u_1 + u_2. \quad (15)$$

This decomposition is a core component of our framework and is applied consistently in both the FDM and FEM settings. To simplify the boundary treatment, we consider the left edge of the domain as the Neumann boundary and the other three edges as Dirichlet boundaries.

### 3.1 FD-CON: Finite Difference Convolutional Operator Network

The FD-CON approach of NICON approximates solutions of Poisson equations by learning to minimize a discretized strong-form residual. In this formulation, the model learns to satisfy the PDE and boundary conditions simultaneously via multiple weighted loss functions. The inputs to the network are

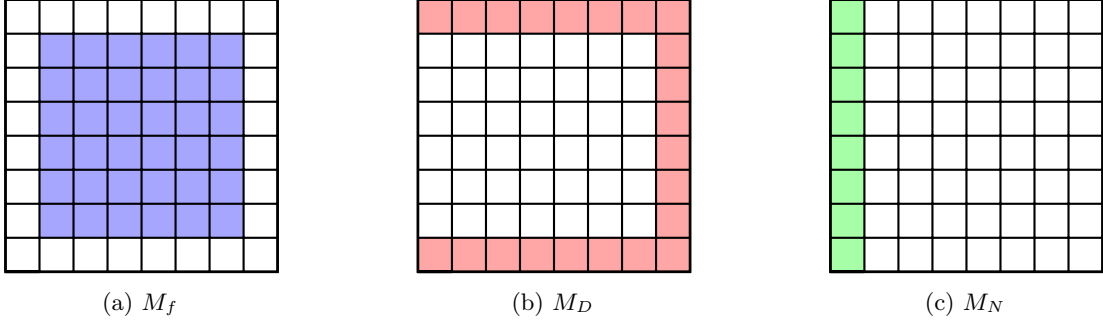


Figure 4: Masks for source term  $M_f$ , Dirichlet boundary  $M_D$ , and Neumann boundary  $M_N$

provided as image channels. As shown in Figure 3, the source term  $f$  is encoded as a dense pixel-wise field over the entire domain  $\Omega$ . In contrast, the Dirichlet and Neumann boundary conditions,  $g_D$  and  $g_N$ , are represented as separate input channels whose pixel values are nonzero only on their respective boundary locations and set to zero elsewhere in the domain. The network predicts the solution over the entire domain. After training, the predicted solution is post-processed by replacing the values on the Dirichlet boundary with the given boundary condition, as illustrated in Figure 3. Therefore, the final solution satisfies the Dirichlet boundary condition exactly while retaining the network prediction in the interior and on Neumann boundaries.

For computational efficiency, we compute the finite difference Laplacian using convolutional kernels. The classical 5-point stencil (2) and 9-point stencil (3) for the discrete Laplacian can be expressed as 2D convolutions with fixed kernels. For example, the discrete Laplacian with the 5-point stencil can be represented as follows:

$$\Delta_h u_{i,j} = \underbrace{\frac{1}{h^2} \begin{bmatrix} 0 & 1 & 0 \\ 1 & -4 & 1 \\ 0 & 1 & 0 \end{bmatrix}}_{=: \alpha_5} * \underbrace{\begin{bmatrix} u_{i-1,j-1} & u_{i-1,j} & u_{i-1,j+1} \\ u_{i,j-1} & u_{i,j} & u_{i,j+1} \\ u_{i+1,j-1} & u_{i+1,j} & u_{i+1,j+1} \end{bmatrix}}_{=: U(i,j)},$$

where  $*$  denotes 2D convolution as used in CNNs. The discrete Laplacian with the 9-point stencil is given by:

$$\Delta_h u_{i,j} = \underbrace{\frac{1}{6h^2} \begin{bmatrix} 1 & 4 & 1 \\ 4 & -20 & 4 \\ 1 & 4 & 1 \end{bmatrix}}_{=: \alpha_9} * \underbrace{\begin{bmatrix} u_{i-1,j-1} & u_{i-1,j} & u_{i-1,j+1} \\ u_{i,j-1} & u_{i,j} & u_{i,j+1} \\ u_{i+1,j-1} & u_{i+1,j} & u_{i+1,j+1} \end{bmatrix}}_{=: U(i,j)}.$$

Then, the discrete Laplacian at  $(i, j)$  can be written in the general form

$$\Delta_h u_{i,j} = \alpha_s (K_s * U(i,j)), \quad s \in \{5, 9\}$$

where  $s$  denotes the stencil size. This formulation provides a unified view of finite difference discretizations and convolutional operators, which we exploit in our model design.

To enforce the governing PDE over the interior of the domain, we define the interior loss by applying a convolution kernel  $K_s$  to the predicted solution  $\hat{U}^k$  and comparing it with the scaled source term  $f^k$ . The loss is evaluated only over a masked region  $M_f$ , which excludes boundary pixels (see Figure 4a):

$$\mathcal{L}_f^k = \frac{1}{|M_f|} \sum_{(i,j) \in M_f} \left| K_s * \hat{U}^k(i,j) + \frac{1}{\alpha_s} f_{i,j}^k \right|^2, \quad (16)$$

where  $|M_f|$  is the number of blue pixels in  $M_f$  and  $\hat{U}^k(i, j)$  denotes the  $3 \times 3$  local stencil extracted from the predicted solution  $\hat{u}^k$  centered at  $(i, j)$ . The scaling factor  $\alpha_s$  increases quadratically as the grid spacing  $h$  decreases. Incorporating such a large factor directly into the convolution kernel can lead to numerically unstable gradients and grid-dependent output scales. To mitigate this, we apply the scaling to the source term  $f$  instead and use the unscaled kernel  $K_s$  during convolution.

To enforce the Dirichlet boundary condition, we define the Dirichlet loss by comparing the predicted solution  $\hat{u}$  with the prescribed boundary data  $g_D$ . The loss is computed only over a masked region  $M_D$ , corresponding to the Dirichlet boundary (see Figure 4b):

$$\mathcal{L}_D^k = \frac{1}{|M_D|} \sum_{(i,j) \in M_D} |\hat{u}_{i,j}^k - g_{D,i,j}^k|^2, \quad (17)$$

where  $|M_D|$  is the number of red pixels in  $M_D$ .

Since we assume that the left boundary of the domain is a Neumann boundary, the Neumann condition (5c) is given by:

$$\nabla_h u(x_i, y_j) \cdot \mathbf{n} = \frac{1}{h} \begin{bmatrix} -1 \\ 1 \end{bmatrix} * \begin{bmatrix} u_{i,j} \\ u_{i,j+1} \end{bmatrix} = g_N(x_i, y_j).$$

Then the loss for the Neumann boundary is given by:

$$\mathcal{L}_N^k = \frac{1}{|M_N|} \sum_{(i,j) \in M_N} |\hat{u}_{i,j+1}^k - \hat{u}_{i,j}^k - h g_{N,i,j}^k|^2, \quad (18)$$

where  $|M_N|$  is the number of green pixels in  $M_N$  (see Figure 4c). As with the interior loss, we avoid including the  $1/h$  factor inside the difference and instead scale  $g_N$  by  $h$  to ensure consistent loss magnitudes across different resolutions.

The total loss is a weighted combination of the three terms:

$$\mathcal{L}_{\text{FDM}} = \frac{1}{N_s} \sum_{k=1}^{N_s} (\lambda_f \mathcal{L}_f^k + \lambda_D \mathcal{L}_D^k + \lambda_N \mathcal{L}_N^k), \quad (19)$$

where  $\lambda_f$ ,  $\lambda_D$  and  $\lambda_N$  are hyperparameters, and  $N_s$  is the number of samples.

In order to train the models for subproblems (13) and (14), each model is trained using only the input channels corresponding to nonzero functions, while zero-valued channels are excluded from the input. More specifically, for Subproblem 1, a two-channel image corresponding to  $f$  and  $g_N$  (see Figures 3a and 3c) is used as the input, and  $g_D = 0$  is enforced in (17). Similarly, for Subproblem 2, a one-channel image corresponding to  $g_D$  (see Figure 3b) is used as the input, and  $f = 0$  and  $g_N = 0$  are enforced in (16) and (18), respectively. When a model predicts the solution, the values on the Dirichlet boundary are post-processed by overwriting with the exact Dirichlet data (see Figure 3d). The boundary values are set using  $g_D$  for both the model problem and Subproblem 2, while the values are set to zero for Subproblem 1.

### 3.2 FE-CON: Finite Element Convolutional Operator Network

The FE-CON approach of NICON extends the FEONet framework [16], which approximates the solution operator mapping the right-hand side vector  $\mathbf{b}$  in the linear system to the finite element solution  $u_h$ . While the MLP-based FEONet directly takes the vector  $\mathbf{f}$  as input, the CNN-based FEONet reshapes  $\mathbf{f}$  into a 2D image-like array to match the input format expected by convolutional layers. Although the

CNN-based FEONet has demonstrated good performance on several examples [16], it suffers from a couple of limitations when applied to non-rectangular or unstructured grids. For example, reshaping  $\mathbf{f}$  into an image format distorts the underlying spatial structure. As a result, neighboring pixels in the image may correspond to spatially distant locations in the actual domain. Moreover, to match the required input format, the mesh must be constructed so that the dimension of  $\mathbf{b}$  matches the number of pixels in the input image, which becomes a severe constraint for domains with complex geometries. In contrast, our method avoids spatial distortion by generating nodes after mapping the domain onto a fixed-size image. As the mesh is constructed from the generated nodes, the dimension of  $\mathbf{b}$  is determined by the image resolution and does not need to be specified in advance (see Figure 2).

FE-CON takes a single-channel image corresponding to  $\mathbf{b}$  as input. Thus, unlike FD-CON, the number of input channels does not change depending on whether Subproblem 1 or Subproblem 2 is being solved. In other words, it remains a single-channel input image in both cases. Specifically, for Subproblem 1, the input image corresponds to  $\mathbf{b}_1$  in (21a), and for Subproblem 2, it corresponds to  $\mathbf{b}_2$  in (21b). After prediction, Dirichlet boundary values are handled in the same way as in FD-CON, that is, the prediction values at the Dirichlet boundary are overwritten with the exact Dirichlet data.

The loss function of FE-CON is identical to that of FEONet [16]. For simplicity, we express it as follows:

$$\mathcal{L}_{\text{FEM}} = \frac{1}{N_s} \sum_{k=1}^{N_s} \|\mathbf{b}^k - A\hat{\mathbf{u}}^k\|_2^2, \quad (20)$$

where  $N_s$  is the number of samples,  $\mathbf{b}^k$  is the  $k$ -th training sample, and  $\hat{\mathbf{u}}^k$  is the FE-CON output corresponding to  $\mathbf{b}^k$ .

One of the ways to justify the decomposition (13)–(14) is through the linear system of equations (10) arising from the FEM formulation. The right-hand side vector  $\mathbf{b}$  in the linear system can be decomposed as  $\mathbf{b} = \mathbf{b}_1 + \mathbf{b}_2$ , where two vectors are defined as follows:

$$(\mathbf{b}_1)_j = \int_{\Omega} f\psi_j \, dx + \int_{\partial\Omega_N} g_N \psi_j \, ds, \quad (21a)$$

$$(\mathbf{b}_2)_j = - \sum_{k=1}^N U_k \int_{\Omega} \nabla \psi_j \cdot \nabla \psi_k \, dx. \quad (21b)$$

Here,  $\mathbf{b}_1$  arises naturally from the variational formulation of FEM, while  $\mathbf{b}_2$  results from the decomposition  $u = w + u_D$  introduced in Section 2. The solution to the linear system in equation (10) can then be expressed as

$$\mathbf{w} = A^{-1}\mathbf{b} = A^{-1}(\mathbf{b}_1 + \mathbf{b}_2) = A^{-1}\mathbf{b}_1 + A^{-1}\mathbf{b}_2.$$

When expressed in the forms of equations (9) and (12),  $A^{-1}\mathbf{b}_1$  corresponds to the solution of Subproblem 1, and  $A^{-1}\mathbf{b}_2 + U_D$  corresponds to the solution of Subproblem 2. For subproblems, the term  $\mathbf{b}$  in the loss function (20) is replaced with  $\mathbf{b}_1$  or  $\mathbf{b}_2$ , depending on the subproblem.

### 3.3 Error Analysis

To simplify the error analysis of NICON (without loss of generality), we consider the Poisson equation with homogeneous Dirichlet boundary conditions, i.e.,  $g_D = 0$  and  $\partial\Omega_D = \partial\Omega$ . We discretize  $\Omega$  by a uniform  $N \times N$  grid with the mesh size  $h = 1/(N-1)$ .

We consider FD-CON first. Let  $\mathcal{V}_I$  be the set of interior grid nodes and  $\mathcal{V}_B$  the set of boundary grid nodes. We reorder the nodes so that interior nodes come first, followed by boundary nodes. Accordingly, a grid function is written as

$$\mathbf{v} = \begin{bmatrix} \mathbf{v}_I \\ \mathbf{v}_B \end{bmatrix} \in \mathbb{R}^{|\mathcal{V}_I| + |\mathcal{V}_B|}, \quad (22)$$

where  $\mathbf{v}_I \in \mathbb{R}^{|\mathcal{V}_I|}$ ,  $\mathbf{v}_B \in \mathbb{R}^{|\mathcal{V}_B|}$ . Let  $A_I \in \mathbb{R}^{|\mathcal{V}_I| \times |\mathcal{V}_I|}$  denote the standard finite difference matrix acting on interior nodes only, obtained from any standard symmetric stencil (e.g., 5-point or 9-point) with homogeneous Dirichlet boundary conditions enforced by elimination. Then  $A_I$  is symmetric positive definite. Importantly, we use the standard scaling in which the interior finite difference operator has the form  $A_I \sim \alpha_s \tilde{A}_I$  where  $\tilde{A}_I$  is an  $h$ -independent stencil matrix. With this convention, the smallest eigenvalue of  $A_I$  is bounded away from zero uniformly in  $h$ , while the largest eigenvalue grows like  $O(h^{-2})$ .

Let us define the (weighted) discrete  $L^2$  inner product and norm on interior node vectors by

$$(\mathbf{v}_I, \mathbf{w}_I)_h := h^2 \mathbf{v}_I^T \mathbf{w}_I, \quad \|\mathbf{v}_I\|_{0,h}^2 := (\mathbf{v}_I, \mathbf{v}_I)_h. \quad (23)$$

Define the discrete  $H^1$ -seminorm by

$$|\mathbf{v}_I|_{1,h}^2 := h^2 \sum_{(i,j) \in \mathcal{V}_I} |\nabla_h v_{i,j}|^2. \quad (24)$$

For homogeneous Dirichlet boundary conditions,  $|\cdot|_{1,h}$  is computed from the interior values with the boundary understood as zero, and it is well known that the associated discrete bilinear form is equivalent to this seminorm:

$$|\mathbf{v}|_{1,h}^2 \simeq h^2 \mathbf{v}_I^T A_I \mathbf{v}_I.$$

More precisely, there exist positive constants  $c_I$  and  $C_I$ , independent of  $h$ , such that for all interior vectors  $\mathbf{v}_I$ ,

$$c_I |\mathbf{v}|_{1,h}^2 \leq h^2 \mathbf{v}_I^T A_I \mathbf{v}_I \leq C_I |\mathbf{v}|_{1,h}^2. \quad (25)$$

For a single input, the FD-CON loss functions (16) and (17) can be written as

$$\mathcal{L}_f = \frac{1}{|\mathcal{V}_I|} \left\| \tilde{A}_I \hat{\mathbf{u}}_I - \frac{1}{\alpha_s} \mathbf{f}_I \right\|_2^2, \quad \mathcal{L}_D = \frac{1}{|\mathcal{V}_B|} \|\hat{\mathbf{u}}_B\|_2^2, \quad (26)$$

where  $\tilde{A}_I = \alpha_s^{-1} A_I$ ,  $\mathbf{f}_I \in \mathbb{R}^{|\mathcal{V}_I|}$  and  $f_j = f(\eta_j)$ ,  $\forall \eta_j \in \mathcal{V}_I$ . Then, we have the following error estimate.

**Theorem 3.1.** *Let  $u \in H^2(\Omega) \cap H_D^1(\Omega)$  be the weak solution, and let  $\hat{\mathbf{u}}$  be the FD-CON prediction. Then there exist positive constants  $C_1$ ,  $C_2$ , and  $C_3$ , independent of  $h$ , such that*

$$|\mathbf{u}_I - \hat{\mathbf{u}}_I|_{1,h}^2 + h^{-1} \|\mathbf{u}_B - \hat{\mathbf{u}}_B\|_{0,h}^2 \leq C_1 h^2 \|u\|_{H^2(\Omega)}^2 + C_2 h^{-4} \mathcal{L}_f + C_3 \mathcal{L}_D, \quad (27)$$

where  $\mathbf{u} = [\mathbf{u}_I^T, \mathbf{u}_B^T]^T$  is the reordered grid function (22) corresponding to the weak solution, i.e.,  $u_j = u(\eta_j)$ ,  $\eta_j \in \mathcal{V}_I \cup \mathcal{V}_B$ ,  $j = 1, \dots, N^2$ .

*Proof.* Clearly,  $\mathbf{u}_B = \mathbf{0}$ . Let  $\mathbf{u}_h^*$  be the finite difference solution, satisfying

$$\mathbf{u}_h^* = \begin{bmatrix} \mathbf{u}_I^h \\ \mathbf{0} \end{bmatrix} \in \mathbb{R}^{|\mathcal{V}_I| + |\mathcal{V}_B|} \quad \text{and} \quad A_I \mathbf{u}_I^h = \mathbf{f}_I.$$

By the triangle inequality, the discrete norm equivalence (25), and the standard finite difference error estimates, we have

$$|\mathbf{u}_I - \hat{\mathbf{u}}_I|_{1,h}^2 \leq 2|\mathbf{u}_I - \mathbf{u}_I^h|_{1,h}^2 + 2|\mathbf{u}_I^h - \hat{\mathbf{u}}_I|_{1,h}^2 \leq Ch^2 \|u\|_{H^2(\Omega)}^2 + 2|\mathbf{u}_I^h - \hat{\mathbf{u}}_I|_{1,h}^2.$$

Cauchy-Schwarz inequality and the discrete Poincaré inequality imply

$$\begin{aligned} |\mathbf{u}_I^h - \hat{\mathbf{u}}_I|_{1,h}^2 &\leq c_I^{-1} h^2 (\mathbf{u}_I^h - \hat{\mathbf{u}}_I)^T A_I (\mathbf{u}_I^h - \hat{\mathbf{u}}_I) \\ &\leq c_I^{-1} h \|\mathbf{u}_I^h - \hat{\mathbf{u}}_I\|_{0,h} \|\mathbf{f}_I - A_I \hat{\mathbf{u}}_I\|_2 \\ &\leq \alpha_s c_I^{-1} C_P h |\mathbf{u}_I^h - \hat{\mathbf{u}}_I|_{1,h} \left\| \tilde{A}_I \hat{\mathbf{u}}_I - \frac{1}{\alpha_s} \mathbf{f}_I \right\|_2. \end{aligned}$$

Since  $\alpha_s \sim h^{-2}$ , we have

$$|\mathbf{u}_I^h - \hat{\mathbf{u}}_I|_{1,h} \leq Ch^{-1} \left\| \tilde{\mathbf{A}}_I \hat{\mathbf{u}}_I - \frac{1}{\alpha_s} \mathbf{f}_I \right\|_2.$$

Combining above results with  $|\mathcal{V}_I| \sim h^{-2}$  yields

$$|\mathbf{u}_I^h - \hat{\mathbf{u}}_I|_{1,h}^2 \leq Ch^2 \|u\|_{H^2(\Omega)}^2 + 2Ch^{-2} \left\| \tilde{\mathbf{A}}_I \hat{\mathbf{u}}_I - \frac{1}{\alpha_s} \mathbf{f}_I \right\|_2^2 \leq Ch^2 \|u\|_{H^2(\Omega)}^2 + 2Ch^{-4} \mathcal{L}_f. \quad (28)$$

By (23) and the fact that  $|\mathcal{V}_B| \sim h^{-1}$ , we have

$$h^{-1} \|\mathbf{u}_B - \hat{\mathbf{u}}_B\|_{0,h}^2 \leq C \frac{1}{|\mathcal{V}_B|} \|\hat{\mathbf{u}}_B\|_2^2 = C \mathcal{L}_D. \quad (29)$$

Combining (28) and (29) concludes the proof.  $\square$

**Corollary 3.2.** *Let  $u^k \in H^2(\Omega) \cap H_D^1(\Omega)$  be the weak solution for  $f^k$ ,  $g_D^k$ , and  $g_N^k$ . Let  $\hat{u}^k \in S \cap H_D^1(\Omega)$  be the FD-CON prediction corresponding to  $f^k$ ,  $g_D^k$ , and  $g_N^k$ . Then*

$$\frac{1}{N_s} \sum_{k=1}^{N_s} \left( |\mathbf{u}_I^k - \hat{\mathbf{u}}_I^k|_{1,h}^2 + h^{-1} \|\mathbf{u}_B^k - \hat{\mathbf{u}}_B^k\|_{0,h}^2 \right) \leq C_1 h^2 \frac{1}{N_s} \sum_{k=1}^{N_s} \|u^k\|_{H^2(\Omega)}^2 + Ch^{-4} \mathcal{L}_{FDM}. \quad (30)$$

**Remark 3.3.** Corollary 3.2 shows that the averaged error consists of an  $O(h^2)$  discretization term and a loss-dependent term scaled by  $h^{-4}$ . Hence, to attain the optimal convergence rate  $O(h^2)$ , the training loss  $\mathcal{L}_{FDM}$  must be bounded by  $O(h^6)$ . For example, halving the mesh size requires reducing  $\mathcal{L}_{FDM}$  by a factor of 64.

We now turn to the FE-CON case. The linear system takes the same form as (10), but  $\mathbf{b}$  is given by

$$b_j = \int_{\Omega} f \psi_j \, dx.$$

Here,  $U = W$  and  $U \in S \cap H_D^1(\Omega)$ .

Let  $M$  denote the global mass matrix defined by

$$M_{ij} = \int_{\Omega} \psi_i \psi_j \, dx. \quad (31)$$

Since the basis functions  $\{\psi_i\}$  are linearly independent, the global mass matrix  $M$  is symmetric positive definite. If  $v_h \in S \cap H_D^1(\Omega)$ , then  $v_h = \sum_{i=1}^N v_i \psi_i$ , where  $v_i = 0$  if  $\eta_i \in \partial\Omega$ . Clearly,  $\nabla v_h = \sum_{i=1}^N v_i \nabla \psi_i$ . Let  $\mathbf{v} = (v_1, \dots, v_N) \in \mathbb{R}^N$ . Then, from (11a) and (31), it follows that

$$\|\nabla v_h\|_{L^2(\Omega)}^2 = \mathbf{v}^T A \mathbf{v} \quad \text{and} \quad \|v_h\|_{L^2(\Omega)}^2 = \mathbf{v}^T M \mathbf{v}. \quad (32)$$

**Lemma 3.4.** *Let  $v_h = \sum_{i=1}^N v_i \psi_i \in S \cap H_D^1(\Omega)$  and  $\mathbf{v} = (v_1, \dots, v_N) \in \mathbb{R}^N$ . If  $\lambda_{min}$  is the minimum eigenvalue of the global mass matrix  $M$ , then*

$$\|\mathbf{v}\|_2^2 \leq \frac{1}{\lambda_{min}} \|v_h\|_{L^2(\Omega)}^2. \quad (33)$$

*Proof.*

$$\|\mathbf{v}\|_2^2 = \frac{1}{\lambda_{min}} \lambda_{min} \mathbf{v}^T \mathbf{v} \leq \frac{1}{\lambda_{min}} \mathbf{v}^T M \mathbf{v} = \frac{1}{\lambda_{min}} \|v_h\|_{L^2(\Omega)}^2.$$

$\square$

Using the above result, we have the following error estimate.

**Theorem 3.5.** *Let  $u \in H^2(\Omega) \cap H_D^1(\Omega)$  be the weak solution and  $\hat{u} \in S \cap H_D^1(\Omega)$  be the FE-CON prediction. Then*

$$\|\nabla u - \nabla \hat{u}\|_{L^2(\Omega)}^2 \leq C_1 h^2 \|u\|_{H^2(\Omega)} + C_2 h^{-2} \|\mathbf{b} - A\hat{u}\|_2^2. \quad (34)$$

*Proof.* Let  $u_h^* \in S \cap H_D^1(\Omega)$  be the finite element solution. The triangle inequality and a priori error estimate of FEM yield

$$\|\nabla u - \nabla \hat{u}\|_{L^2(\Omega)}^2 \leq Ch^2 \|u\|_{H^2(\Omega)}^2 + 2\|\nabla u_h^* - \nabla \hat{u}\|_{L^2(\Omega)}^2.$$

By Cauchy-Schwarz inequality, the discrete Poincaré inequality, (32), and (33), we have

$$\begin{aligned} \|\nabla u_h^* - \nabla \hat{u}\|_{L^2(\Omega)}^2 &\leq \|\mathbf{u}_h^* - \hat{u}\|_2 \|\mathbf{b} - A\hat{u}\|_2 \\ &\leq \frac{C_P}{\sqrt{\lambda_{\min}}} \|\nabla u_h^* - \nabla \hat{u}\|_{L^2(\Omega)} \|\mathbf{b} - A\hat{u}\|_2 \end{aligned}$$

Since  $\lambda_{\min} \geq C_M h^2$ , we have

$$\|\nabla u_h^* - \nabla \hat{u}\|_{L^2(\Omega)} \leq Ch^{-1} \|\mathbf{b} - A\hat{u}\|_2.$$

Combining the above results concludes the proof.  $\square$

**Corollary 3.6.** *Let  $u^k \in H^2(\Omega) \cap H_D^1(\Omega)$  be the weak solution for  $f^k$ ,  $g_D^k$ , and  $g_N^k$ . Let  $\hat{u}^k \in S \cap H_D^1(\Omega)$  be the FE-CON prediction corresponding to  $\mathbf{b}^k$ . Then*

$$\frac{1}{N_s} \sum_{k=1}^{N_s} \|\nabla u^k - \nabla \hat{u}^k\|_{L^2(\Omega)}^2 \leq C_1 h^2 \frac{1}{N_s} \sum_{k=1}^{N_s} \|u^k\|_{H^2(\Omega)}^2 + C_2 h^{-2} \mathcal{L}_{FEM}. \quad (35)$$

In Corollary 3.6, the left-hand side is the average of the squared  $H^1$ -seminorm error over the training set. Thus, if the loss  $\mathcal{L}_{FEM}$  is sufficiently small, the average of squared error is bounded by  $O(h^2)$ .

**Remark 3.7.** *To attain the optimal rate of convergence over the training set,  $\mathcal{L}_{FEM}$  must be bounded by  $O(h^4)$ . This suggests a strategy for training. If  $\mathcal{L}_{FEM} = L_c$  when  $h = h_c$ , then FE-CON should be trained until  $\mathcal{L}_{FEM} \leq L_c/16$  when  $h = h_c/2$ .*

**Remark 3.8.** *In [11], the error is decomposed into the FEM error, approximation error, and generalization error. In particular, Theorem 4.10 bounds the approximation and generalization errors by  $\kappa(A)^{1+d}/\sqrt{n}$  and  $\kappa(A)^{1+3d/2}/\sqrt{M}$ , respectively, where  $\kappa(A)$  is the condition number of the finite element system matrix,  $d$  is the spatial dimension,  $n$  is the hidden-layer width, and  $M$  is the number of training samples. Since  $\kappa(A) = O(h^{-2})$  when  $d = 2$ , these bounds grow rapidly under mesh refinement, suggesting potentially pessimistic scaling on fine meshes. By contrast, our analysis bounds the error in terms of the FEM error and the residual-based loss, without explicitly separating approximation and generalization components.*

## 4 Numerical Experiments

In this section, we evaluate NICON on elliptic PDEs in a data-free physics-informed operator learning setting. In this setting, the models are trained without paired input–output data by minimizing residual-based losses.

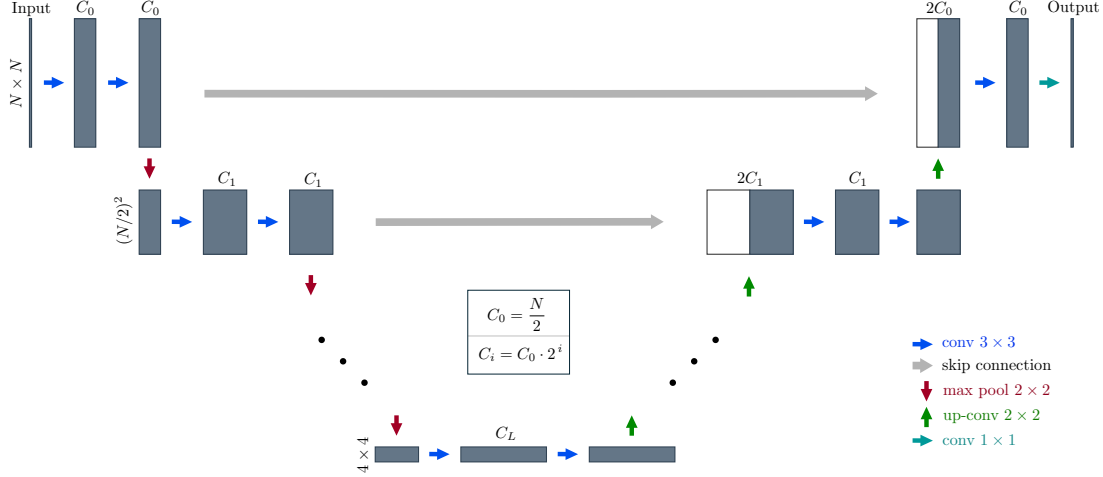


Figure 5: Resolution-dependent U-Net architecture for NICON.

#### 4.1 Network Architecture and Experimental Setup

Within the NICON framework, the choice of network architectures is not restricted, and in principle any fully convolutional network can be employed. In this work, we adopt a U-Net-style network because its encoder–decoder structure with skip connections is well suited for capturing multiscale features in input images. Through the proposed domain-to-image mapping, this property is expected to facilitate the approximation of multiscale structures in PDE solutions.

The architecture is parameterized by two hyperparameters: the base channel size  $C_0$  and the network depth  $L$ , which are chosen as explicit functions of the grid resolution  $N$  in order to control the model capacity. The network consists of  $L$  encoder blocks, a bottleneck block, and  $L$  decoder blocks. At encoder level  $i = 0, \dots, L-1$ , the number of feature channels is given by

$$C_i = C_0 \cdot 2^i.$$

Each encoder block contains two  $3 \times 3$  convolution layers with ReLU activations, followed by a  $2 \times 2$  max-pooling operation for spatial downsampling. The feature maps from the encoder blocks are stored and later used as skip connections.

At the smallest resolution, a bottleneck block with channel dimension  $C_0 \cdot 2^L$  is applied, consisting of two  $3 \times 3$  convolution layers with ReLU activations. The decoder is symmetric to the encoder in structure: at each depth, feature maps are upsampled using a  $2 \times 2$  transposed convolution, concatenated with the corresponding encoder feature map, and processed by two  $3 \times 3$  convolution layers with ReLU activations. A final  $1 \times 1$  convolution maps the decoder output to a single-channel field defined on the computational grid. To ensure that the expressive capacity of the network increases systematically with the grid resolution, the base channel size and depth are fixed according to the following *a priori* rule:

$$C_0 = \frac{N}{2}, \quad L \in \{2, 3, 4, 5\} \text{ for } N \in \{16, 32, 64, 128\}.$$

Under this scaling rule, the spatial resolution at the bottleneck is reduced to  $4 \times 4$  for all grid sizes. This rule is applied uniformly across all experiments and models. No architecture-specific tuning is performed for individual problem settings.

The same network architecture is used for all FD-CON and FE-CON models. Differences between discretizations appear only in the number and interpretation of input channels, while the network

structure and capacity scaling remain identical. This design ensures that the number of learnable parameters grows consistently with the spatial resolution and preserves the same architectural pattern across all experiments.

Unless otherwise mentioned, all experiments are conducted under the same experimental setting. The Adam optimizer is used with an initial learning rate of  $10^{-4}$ , combined with a cosine decay schedule over the entire training horizon. All experiments are trained for 10,000 epochs with a batch size of 32. Training is performed in single-precision arithmetic (float32), and model checkpoints are selected based on the minimum training loss. All experiments are conducted on an Ubuntu 22.04 system equipped with an NVIDIA RTX A6000 GPU with 48 GB of memory, and the models are implemented in Python using JAX.

We consider the Poisson problem (1) on the unit square  $\Omega = (0, 1)^2$ , with a Neumann condition on the left boundary and Dirichlet conditions on the remaining boundaries. We use a fixed training set of 3,000 samples and an independent test set of 1,000 samples, and keep hyperparameter settings fixed and identical across grid sizes and models. The source term  $f$  and boundary data  $(g_D, g_N)$  are sampled independently from randomized smooth sinusoidal functions:

$$\phi(x, y) = a_1 \sin(b_1 x + b_2 y) + a_2 \cos(b_3 x + b_4 y),$$

where  $f$ ,  $g_D$ , and  $g_N$  are generated independently from this function class, with  $a_1, a_2, b_1, \dots, b_4 \in [0, 5] \subseteq \mathbb{R}$  sampled independently. This choice of the function class follows the setup used in [16] and provides a convenient and widely used benchmark for operator learning methods. This independent sampling avoids spurious correlations between interior and boundary inputs and exposes the models to fully varying mixed boundary conditions. This setting goes beyond homogeneous Dirichlet problems and exposes the models to fully varying interior and boundary inputs. When an experiment deviates from this default setting, we explicitly state the differences at the beginning of the corresponding subsection.

Experiments are conducted on  $N \times N$  grids, where  $N \in \{16, 32, 64, 128\}$ . Reference solutions are computed on a sufficiently fine grid (approximately  $1024 \times 1024$ ) using a classical FEM and are used only for evaluation. We consider four models: FD-CON with a 5-point stencil (FD-5) and a 9-point stencil (FD-9), and FE-CON with triangular elements (FE-T) and rectangular elements (FE-R). For each grid size  $N$ , the model capacity is scaled proportionally to  $N$  according to a fixed, a priori rule that is applied uniformly across all models and experiments, and is not optimized for individual settings. For the decomposed formulation, each subproblem model matches the architecture and capacity of the corresponding original (non-decomposed) model at the same grid resolution. Each model is trained using its corresponding loss function (19) for FD-CON and (20) for FE-CON. For FD-CON, the loss weights are fixed as  $\lambda_f = \lambda_D = \lambda_N = 1$  throughout the experiments for simplicity; the optimal choices for the loss weights are left for future work. We define the relative error of a prediction  $v$  with respect to the reference solution  $u_h^*$  by

$$\text{Rel}_{H^1}(v) := \frac{\|u_h^* - v\|_{H^1(\Omega)}}{\|u_h^*\|_{H^1(\Omega)}}.$$

This metric is used consistently to evaluate the accuracy of all models.

Figure 6 shows the computational workflow of FD-CON. The PDE data  $f$ ,  $g_N$ , and  $g_D$  are first transformed by the domain-to-image mapping, so that each input image encodes not only the values of the data but also the geometry of the domain and the boundary information. For FD-CON, these images are used directly as network inputs. In the original problem, the model takes a three-channel input image that consists of  $f$ ,  $g_N$ , and  $g_D$ . In the subproblems, two separate models are used: the model for Subproblem 1 uses a two-channel input image corresponding to  $f$  and  $g_N$ , while the model for Subproblem 2 uses a single-channel input image corresponding to  $g_D$ . Each model produces a

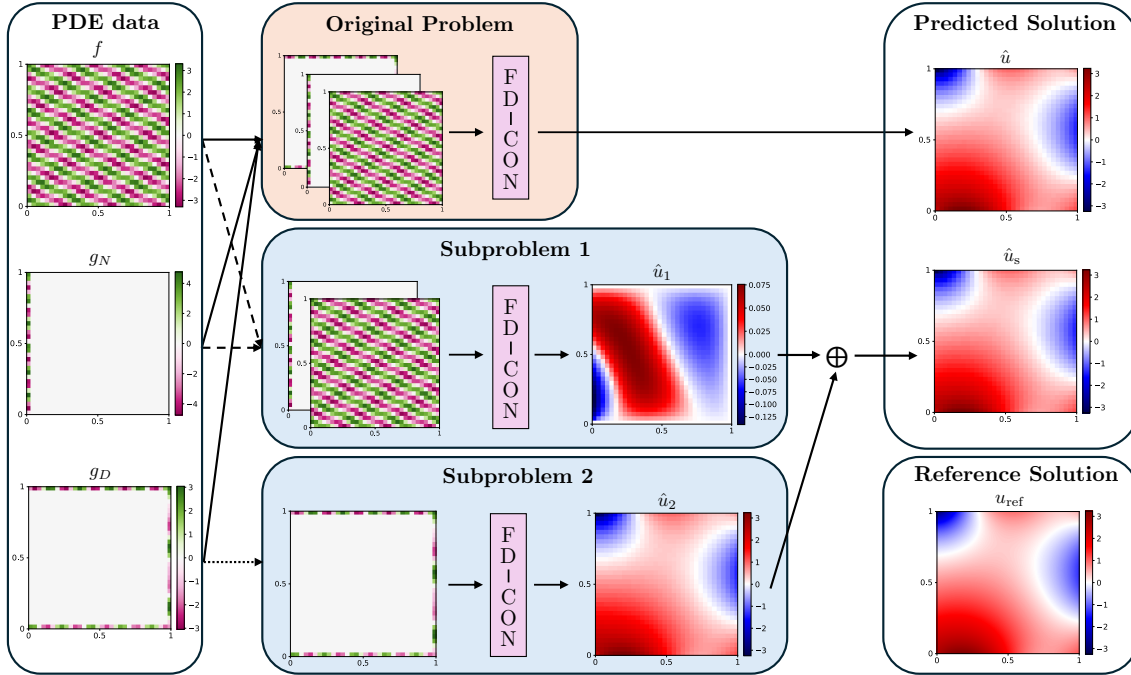


Figure 6: Computational workflow of FD-CON for  $N = 32$ .

corresponding prediction,  $\hat{u}$ ,  $\hat{u}_1$ , and  $\hat{u}_2$ , respectively, and the final prediction of the decomposed problem is obtained as  $\hat{u}_s = \hat{u}_1 + \hat{u}_2$ .

For FE-CON, the PDE data are first mapped to a mesh through the domain-to-image mapping. Then, the right-hand side vectors defined in (11b), (21a), and (21b) are reshaped into image representations and used as inputs for the original problem, Subproblem 1, and Subproblem 2, respectively. Unlike FD-CON, all FE-CON models take a single-channel image as input. The predictions are denoted in the same manner as for FD-CON. The corresponding computational workflow for FE-CON is illustrated in Figure 12, and is discussed in more detail in Section 4.5 in the context of a different example.

## 4.2 Performance Evaluation for Poisson Problem

We begin by evaluating NICON under the default experimental setting described above. The evaluation focuses on the convergence of the relative  $H^1$  error under grid refinement and on a comparison between the original and decomposed formulations. On the training set, we observe near-optimal convergence across all models, with the decomposed formulation performing better in most cases. In particular, the relative  $H^1$  error decreases at an approximately first-order rate with respect to grid refinement, as indicated by the reference triangle in Figure 7a. This behavior is consistent across finite difference and finite element methods and suggests that the proposed models remain robust under mixed boundary conditions.

In contrast, the test errors shown in Figure 7b are generally larger than the corresponding training errors. While the test error decreases as the grid is refined from coarse grids up to  $N = 64$ , it shows a noticeable increase at  $N = 128$ , which results in a clear gap between training and test errors. Notably, the decomposed formulation produces smaller test errors and reduces the increment observed at  $N = 128$ , which indicates improved generalization on fine grids. These results suggest that, although the residual-based training objective can be optimized to achieve near-optimal convergence on the

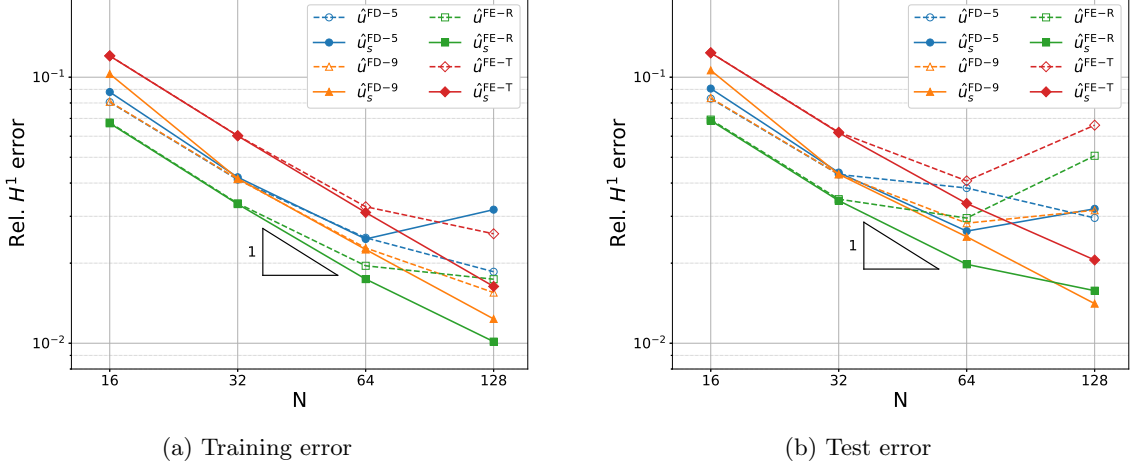


Figure 7: Convergence of the relative  $H^1$  error under grid refinement. The error is plotted against increasing grid size  $N$ . The reference triangle indicates the optimal convergence rate. Results show the mean over five random seeds.

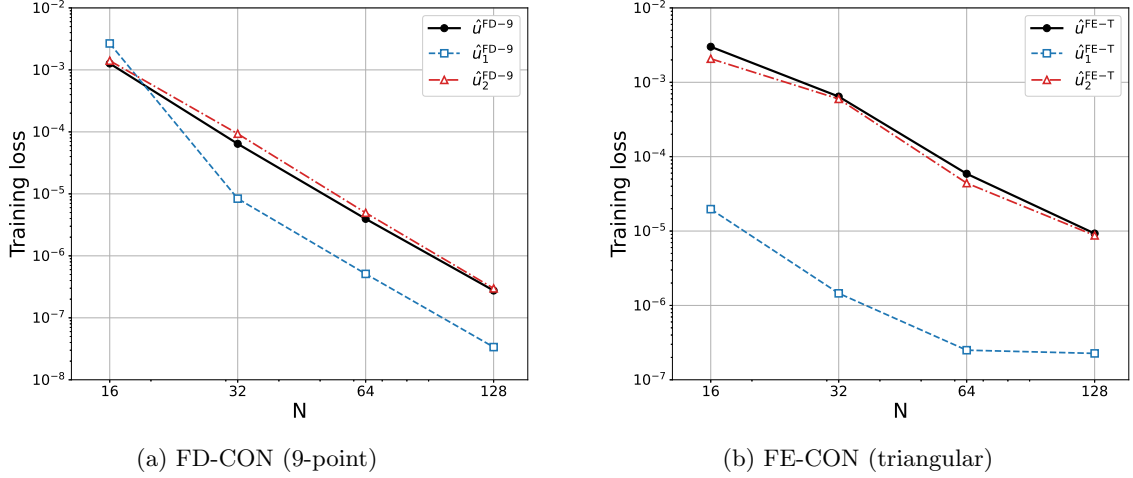


Figure 8: Best training loss under grid refinement for the original and decomposed formulations. Within each discretization, we compare the original predictor and the two subproblem predictors. Results are averaged over five random seeds.

training set, generalization becomes increasingly challenging as the grid size increases.

Figure 8 shows that the training loss behavior of the subproblem models is not uniformly better than that of the non-decomposed formulation. In particular, for the FD-9, the training loss of the model for Subproblem 2 ( $\hat{u}_2^{FD-9}$ ) is comparable to that of the model for the original problem ( $\hat{u}^{FD-9}$ ). This result indicates that learning Subproblem 2 can be as challenging as learning the full operator from the perspective of optimization. Nevertheless, Figure 7 shows that decomposition consistently improves generalization under grid refinement. Even when the training loss of the decomposed formulation is comparable to that of the original formulation, the decomposed formulation yields lower test errors

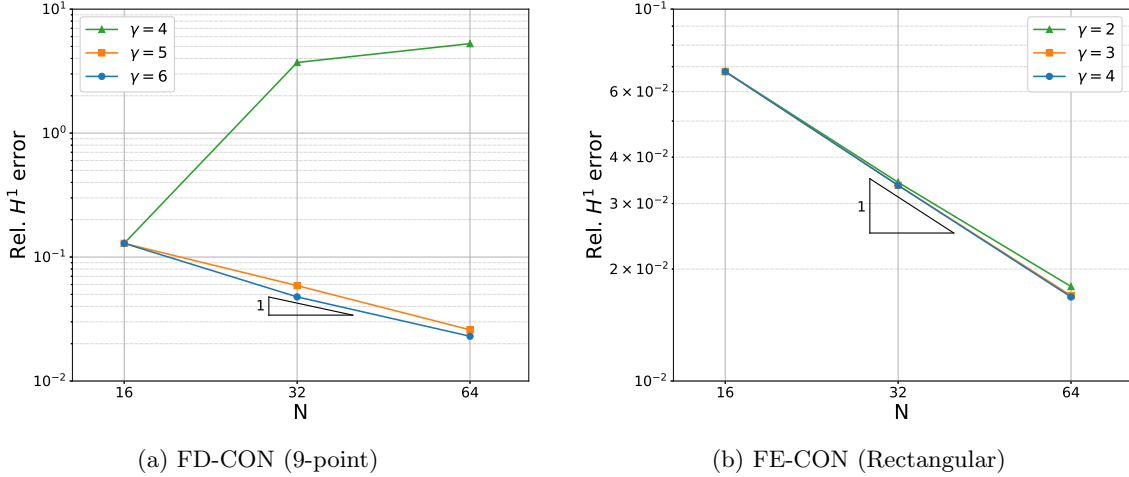


Figure 9: Relative  $H^1$  errors for FD-CON and FE-CON for different loss scalings ( $O(h^\gamma)$ ).

across discretizations. This observation suggests that the benefit of decomposition does not arise solely from easier optimization. Instead, it arises from learning structurally simpler sub-operators whose composition yields better generalization of the full solution operator.

### 4.3 Numerical Verification of Error Estimates and Generalization

In Section 4.2, all models are trained using the same experimental setup, with a fixed number of training samples and identical hyperparameter settings across grid sizes. Under this setting, Figure 7 shows that the training error does not always exhibit the optimal convergence rate expected from classical FDM and FEM theory, and in some cases even increases as the grid is refined. According to Corollary 3.2 and Remark 3.3 (resp. Corollary 3.6 and Remark 3.7), achieving the optimal convergence rate for FD-CON (resp. FE-CON) requires the training loss  $\mathcal{L}_{\text{FDM}}$  (resp.  $\mathcal{L}_{\text{FEM}}$ ) to decrease at a rate that depends explicitly on the grid size. More precisely, when the grid size parameter  $N_s$  is doubled (equivalently,  $h \mapsto h/2$ ), training should be continued until

$$\mathcal{L}_{\text{FDM}}(2N_s) \leq \mathcal{L}_{\text{FDM}}(N_s)/64 \quad (\text{resp. } \mathcal{L}_{\text{FEM}}(2N_s) \leq \mathcal{L}_{\text{FEM}}(N_s)/16),$$

for the optimal convergence rate. Figure 9 shows that the training error converges at the optimal rate with the above stopping criterion. In particular, the theoretically guaranteed loss scalings lead to consistently optimal convergence behavior, while slightly weaker scalings still yield near-optimal rates. In contrast, insufficient loss decay results in degraded convergence or even training failure with the theoretical analysis.

Building on the theoretical result in FEONet [11], which states that the generalization error scales as  $O(N_s^{-1/2})$ , our results in Figure 10 show a consistent dependence on the sample size. In our training setting, the training set size is fixed at 3,000 samples. As a result, the training loss can be reduced to the level required by the stopping criterion, and the training error can recover the optimal convergence behavior under grid refinement. However, this does not necessarily guarantee the optimal convergence rate on the test set, as also observed in Figure 7. One key reason is that increasing the grid parameter  $N$  enlarges the U-Net architecture and increases the number of trainable parameters. Therefore, a fixed and relatively small training set may be insufficient to constrain the model appropriately at finer resolutions. Figure 10 supports this interpretation. The training loss decreases consistently as the number of training samples increases for both  $N = 32$  and  $N = 64$ , whereas the test error

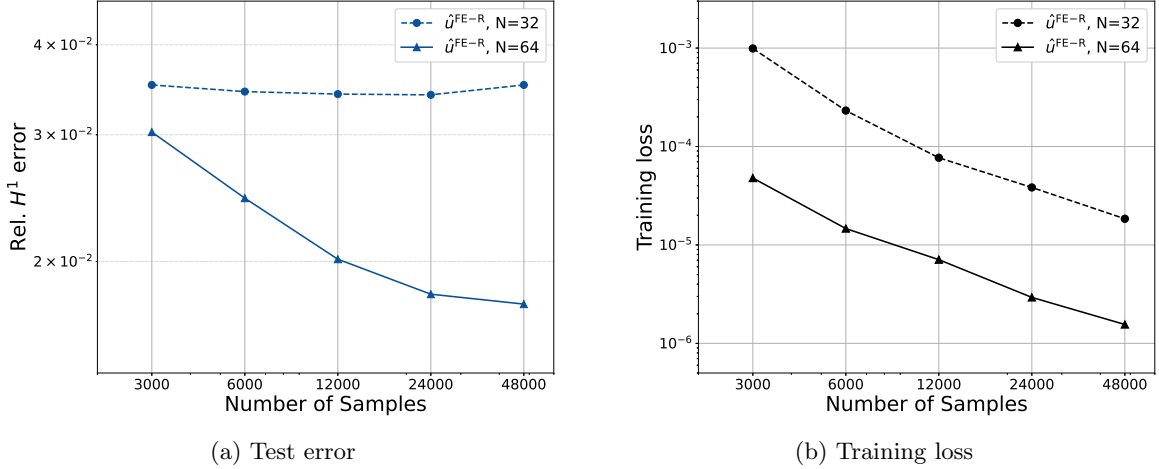


Figure 10:  $H^1$  error on the test set and training loss versus the number of training samples.

shows qualitatively different behaviors across resolutions. For  $N = 32$ , the test error remains nearly unchanged as the number of training samples increases, whereas for  $N = 64$  it decreases consistently and eventually reaches roughly half of the error level observed at  $N = 32$ . This behavior is consistent with the magnitude expected when moving from  $N = 32$  to  $N = 64$  under optimal convergence. These results suggest that achieving the optimal convergence rate on the test set requires not only sufficient optimization, as ensured by the stopping criterion, but also a training sample size that grows with the effective problem complexity at larger  $N$ . This complexity can be influenced by factors such as the increase in the number of trainable parameters and the conditioning of the underlying FEM system.

**Remark 4.1** (Comparison with [11]). *The different theoretical results (see Remark 3.8) are also reflected in numerical behavior. In [11], numerical experiments for a one-dimensional convection-diffusion equation show that the theoretical upper bounds begin to increase even for relatively coarse meshes. In contrast, our experiments are conducted on two-dimensional problems with the number of elements scaling as  $(N - 1)^2$ , yet we observe stable and monotone convergence even on fine grids. One plausible factor behind the different empirical behavior is optimization difficulty. In [11], the number of trainable parameters typically grows with both network width and depth, which can make it harder to drive the training loss to the level needed for stable behavior under mesh refinement. In contrast, we use a U-Net architecture without fully connected layers and further reduce the learning complexity via subproblem decomposition, which together improve training stability on fine meshes.*

#### 4.4 Training Efficiency via Problem Decomposition

We study training efficiency using FE-CON with rectangular elements (FE-R) as a representative example; the same qualitative trends were observed for the other models. This experiment follows the default Poisson setting described in Section 4, except for the training–testing setting. First, we independently sample two marginal input sets corresponding to the two subproblems, one for the input pair  $(f, g_N)$  and the other for  $g_D$ , and consider all possible combinations of these inputs as potential joint inputs. This setting reflects scenarios in which the number of possible joint inputs grows combinatorially with the number of varying input components. Next, the original (non-decomposed) formulation is trained using a subset of these joint input combinations, whereas the decomposed formulation is trained separately on the two marginal input sets and never observes any paired combinations during training.

We compare the decomposed and non-decomposed formulations under a common evaluation setting

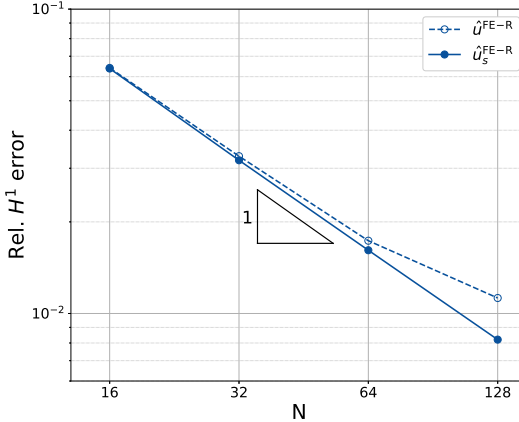


Figure 11: Decomposition-based learning improves data efficiency for FE-CON with rectangular elements (FE-R) by composing independently learned subproblem predictions at inference.

based on joint input combinations. The two subproblems follow the decomposition in (13)–(14), with inputs  $(f, g_N)$  and  $g_D$ , respectively. Two independent input sets of size 100, corresponding to the two subproblems, define a pool of 10,000 possible joint input combinations. From this pool, 5,000 combinations are sampled uniformly at random to form the training set for the original (non-decomposed) formulation, while the remaining 5,000 disjoint combinations are used as a common test set for both formulations. All experiments use the same underlying input functions and the same train–test split across grid sizes.

In the original formulation, the operator is trained on the 5,000 joint input combinations using the same optimizer and hyperparameter settings as in the default setting. In contrast, the decomposed formulation trains two subproblem models using only 200 independent inputs in total (100 per subproblem) and does not observe any joint input combinations during training. Each subproblem model is trained independently, typically for a substantially larger number of optimization steps than the original formulation. This reflects the lower-dimensional and structurally simpler learning task associated with each subproblem.

Figure 11 shows the performance of the original and decomposed formulations for FE-CON with rectangular elements. Although the decomposed formulations are trained on significantly fewer samples, they consistently achieve lower relative  $H^1$  errors across all grid resolutions, which indicates superior accuracy. This behavior can be explained in part by the combinatorial structure induced by decomposition. Training on marginal input sets implicitly covers all joint input combinations generated by their composition. As a result, the joint inputs used for testing can be regarded as being effectively included in the training samples of the decomposed formulation. Therefore, this setting highlights the training efficiency benefits of decomposition in terms of effective sample coverage.

Importantly, this effect does not apply to the experiments in Section 4.2, where the test inputs are not implicitly covered by the training samples of the decomposed formulation. The consistently improved performance of the decomposed model observed in Section 4.2 suggests that, even without such coverage, decomposition allows the same number of training samples to be used more effectively by distributing them across simpler subproblems. In this sense, decomposition provides an effect analogous to training on a substantially larger and more diverse set of training samples, which leads to improved generalization.

These results show that problem decomposition can substantially improve training efficiency by

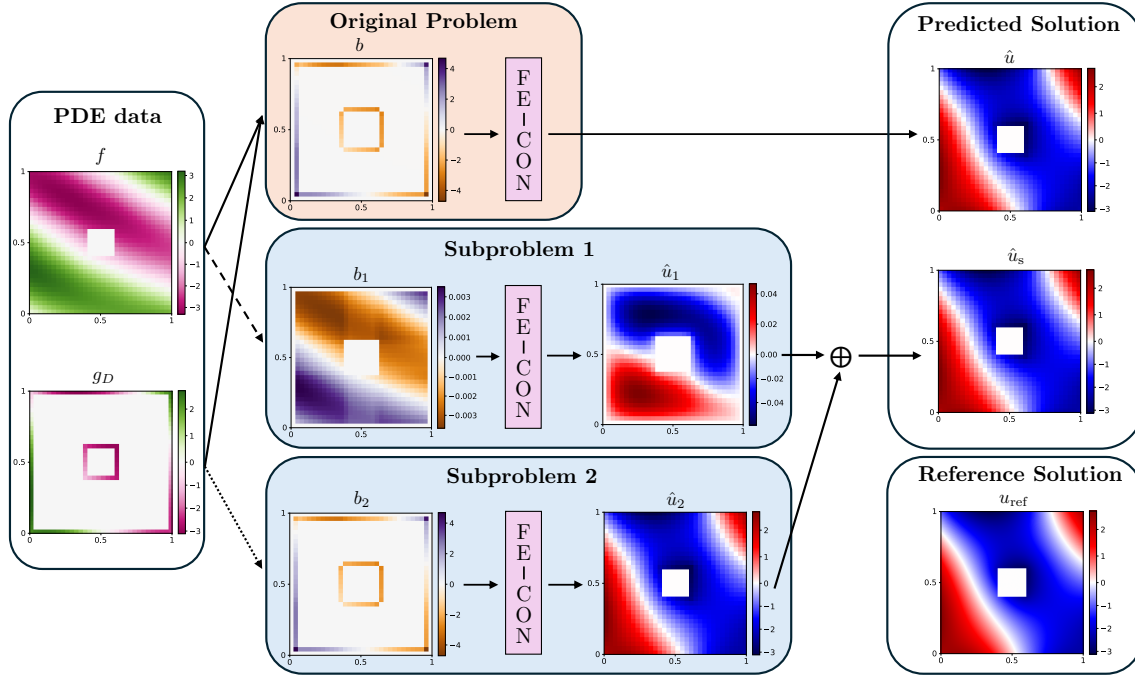


Figure 12: Computational workflow of FE-CON on a complex geometry (36) for  $N = 32$ .

exploiting the compositional structure of the solution operator. Although the decomposed formulation requires multiple sub-operator models, each subproblem is lower-dimensional or structurally simpler. This property leads to more stable and reliable training than directly learning the full operator from a large set of training samples. By learning sub-operators independently and composing them during inference, the decomposed approach uses a fixed number of training samples more effectively and provides a more practical alternative in realistic scenarios where training with a large training set is costly or unstable.

#### 4.5 Extension to Complex Geometry

We further examine the proposed method on a complex domain. This experiment differs from the default setting in Section 4 in two aspects. First, we consider a square domain containing a square hole,

$$\Omega = (0, 1)^2 \setminus [0.4, 0.6]^2. \quad (36)$$

Second, we impose the nonhomogeneous Dirichlet boundary conditions on both the outer and inner boundaries.

Figure 12 illustrates the computational workflow of FE-CON. In FE-CON, a single-channel image corresponding to the right-hand side vector in the FE system is used as the network input. As shown in the figure, when the magnitudes of  $f$  and  $g_D$  are comparable, the original problem becomes more challenging to learn. This difficulty can be explained by the construction of the input. According to (21a), the contributions of  $f$  and  $g_N$  are obtained through integrations over the domain  $\Omega$  and the Neumann boundary  $\partial\Omega_N$ , respectively. Since the basis function  $\psi$  has local support, the resulting integrals decrease as  $N$  increases. In contrast, the integration in (21b) is independent of the mesh size  $h$ , and hence it remains unchanged as  $N$  increases. As a result,  $b_2$  becomes dominant for finer grids. This behavior explains why  $b$  and  $b_2$  appear nearly indistinguishable in Figure 12. By decomposing the

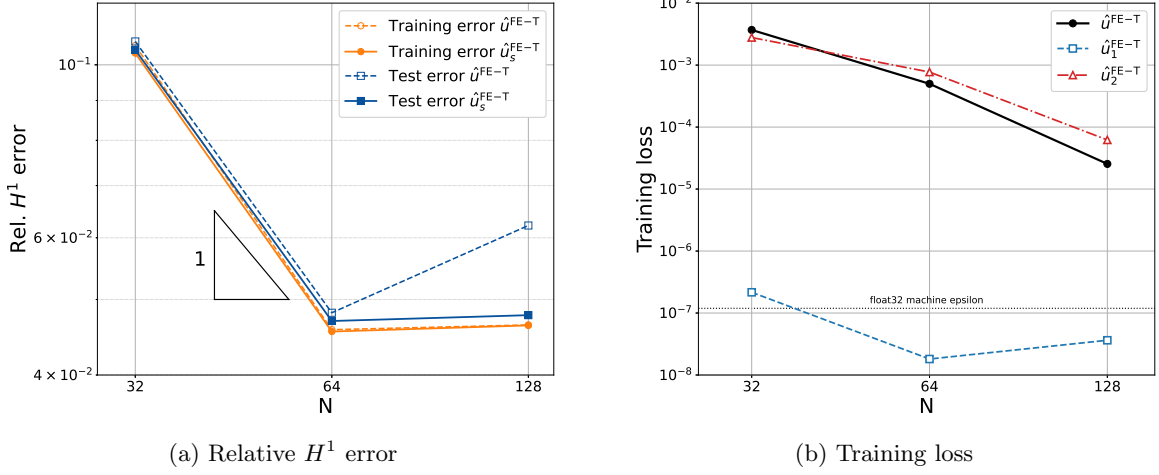


Figure 13: Relative  $H^1$  error and residual-based training loss across grid sizes on the square-hole domain.

original problem into subproblems and treating these components separately, the proposed decomposition avoids this unfavorable scaling imbalance. Consequently, the decomposition yields a more balanced learning problem and leads to improved numerical robustness.

Figure 13a shows the relative  $H^1$  error with respect to the reference finite element solutions. As  $N$  increases from 32 to 64, the errors for both the training and test sets decrease for all models. When  $N$  increases further to 128, the decomposed formulation shows only a slight increase in the relative  $H^1$  error, whereas the integrated model exhibits a noticeable increase in the test error. Figure 13b shows the training loss. Under the decomposed formulation, the loss for subproblem 1 reaches the float32 precision floor for  $N \geq 64$ , which suggests that further reduction is limited by finite-precision arithmetic. The loss for subproblem 2 continues to decrease, but this decrease does not lead to a smaller  $H^1$  error at  $N = 128$ .

In general, even if the source term and Dirichlet boundary conditions are smooth, the weak solution can have corner singularities near reentrant corners. As a result, the solution may not have sufficient regularity for the optimal convergence rate. On sufficiently fine grids, the relative  $H^1$  error is largely determined by  $\hat{u}_2$ , together with corner singularities. However, the observed convergence rate from  $N = 32$  to  $N = 64$  is higher than the first-order rate ( $\approx 1$ ) that is expected when the solution is sufficiently smooth. This behavior suggests that the experiment is still in a pre-asymptotic regime. For finer grids, the error becomes increasingly influenced by the corner singularities, so further refinement from  $N = 64$  to  $N = 128$  can yield only marginal improvement or even a slight increase in the measured error.

The increase in the test error of the integrated model at  $N = 128$  is better explained by generalization than by optimization. The number of training samples is fixed across  $N$ , while the model complexity increases with  $N$ . This can enlarge the generalization gap, as shown in Figure 7. This issue can be reduced by increasing the number of training samples at larger  $N$ , as shown in Figure 10.

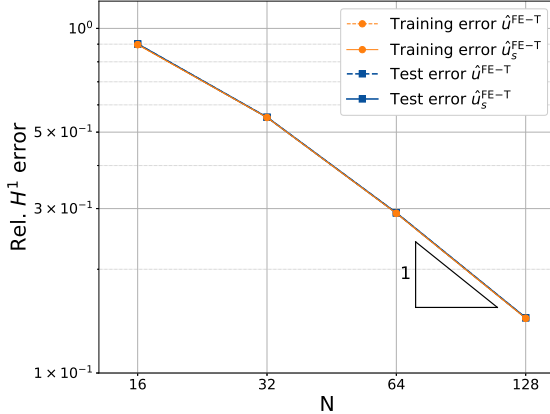


Figure 14: Relative  $H^1$  error for the Helmholtz problem (37) under uniform grid refinement.

#### 4.6 Extension to Helmholtz Equation

To assess the applicability of the proposed method beyond the Poisson problem, we consider the Helmholtz equation given by

$$\Delta u + \kappa^2 u = f \quad \text{in } \Omega, \quad (37a)$$

$$u = g_D \quad \text{on } \partial\Omega, \quad (37b)$$

where  $\Omega = (0, 1)^2$  and  $\kappa = 1$ , and

$$f(x, y) = -(a_1\pi)^2 \sin(a_1\pi x) \sin(a_2\pi y) - (a_2\pi)^2 \sin(a_1\pi x) \sin(a_2\pi y) + \kappa^2 \sin(a_1\pi x) \sin(a_2\pi y), \quad (38)$$

is a forcing term for which the exact solution is given by

$$u(x, y) = \sin(a_1\pi x) \sin(a_2\pi y). \quad (39)$$

Helmholtz problems of this form have been considered in the physics-informed learning literature [21, 28]. In this work,  $a_1, a_2 \in [1, 20]$  are sampled independently and the nonhomogeneous Dirichlet boundary condition (37b) is prescribed by the trace of the exact solution,  $g_D = u|_{\partial\Omega}$ . This setting admits solutions with highly oscillatory behavior over a wide range of parameters and nonhomogeneous Dirichlet conditions. For evaluation, the exact solution  $u$  in (39) is sampled on a sufficiently fine grid (approximately  $1024 \times 1024$ ), and the resulting discrete solution is used as the reference solution  $u_h^*$  for computing the relative  $H^1$  error. Except for the above definition of the problem data, all other experimental settings are identical to those used in the Poisson experiments.

Figure 14 shows the relative  $H^1$  error for the Helmholtz problem under uniform grid refinement. The errors for both the training and test sets decrease consistently as the grid is refined, and their magnitudes remain comparable across all resolutions. These results show that, under the present setting, the proposed networks are able to capture the solution operator for the Helmholtz problem without a generalization gap.

Figure 15 shows representative approximate solutions produced by FE-CON for the Helmholtz problem, together with the source term  $f$  and the corresponding reference solution, for  $N = 16, 32, 64, 128$ . In this case, the Dirichlet boundary data  $g_D$  is prescribed as the boundary of the reference solution. As shown in the figure, the solution exhibits anisotropic oscillatory behavior: it varies slowly in the  $x$ -axis

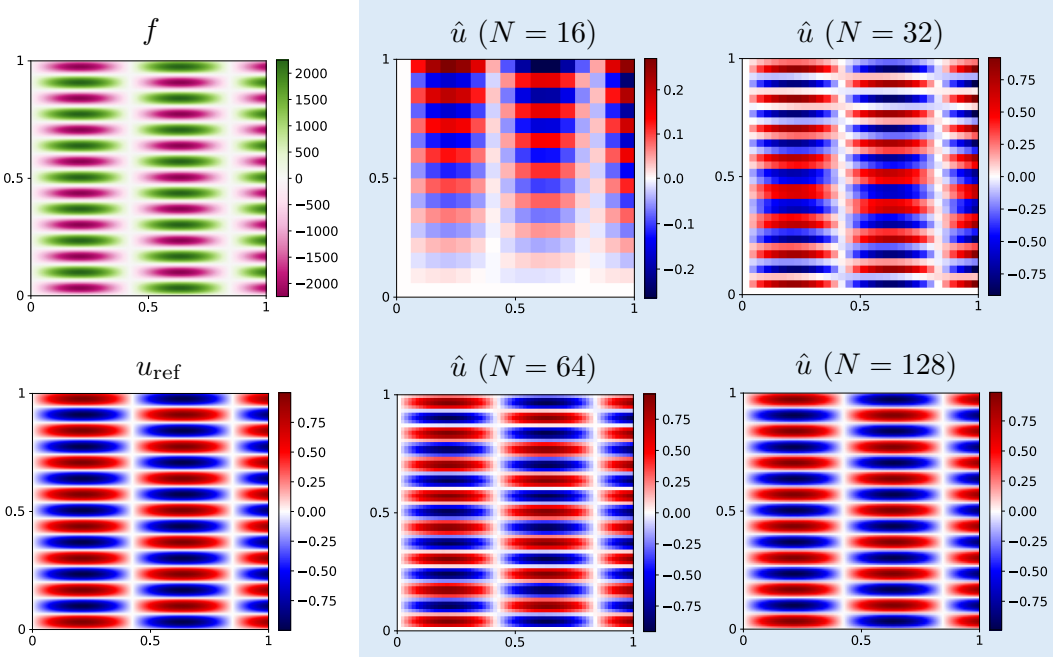


Figure 15: FE-CON approximations for the Helmholtz problem at  $N = 16, 32, 64, 128$ .

direction while displaying rapid oscillations in the  $y$ -axis direction. Such strongly oscillatory features are difficult to resolve on coarse grids. For  $N = 16$  and  $N = 32$ , the FE-CON predictions do not accurately capture the fine-scale oscillations of the reference solution. As the grid is refined, the quality of the predicted solutions improves significantly. For  $N = 64$  and  $N = 128$ , FE-CON produces approximations that closely match the reference solution and correctly represent the oscillatory structure.

These results indicate that, when the solution exhibits fine-scale variations, an operator network must be able to represent and predict solutions on sufficiently fine grids. The present experiment shows that FE-CON possesses this capability under grid refinement, even for Helmholtz problems with highly oscillatory solutions.

## 5 Conclusion

In this work, we developed a numerically informed operator learning framework, called NICON, that explicitly couples classical finite difference and finite element methods with operator learning through residual-based training loss functions. We introduced two types of networks, FD-CON and FE-CON, which use residual-based loss functions derived from finite difference and finite element formulations, respectively. Both approaches remain compatible with standard convolutional neural network architectures. To address spatial distortion that occurs when vector-valued data generated on nonuniform grids are reshaped into image-like matrix representations, we adopted a domain-to-image mapping approach. This approach generates input data on a fixed image resolution. As a result, input and output fields admit consistent representations and the geometric information of the domain is preserved independently of grid size. Using finite difference and finite element analysis, we derived error estimates for FD-CON and FE-CON. These estimates relate the convergence behavior directly to the decay rate of the training loss. Based on these analyses, we established training strategies that guarantee optimal convergence rates under grid refinement. Numerical experiments validated

the theoretical results and showed that the proposed framework remains stable and accurate on fine grids. In particular, FD-CON and FE-CON achieve reliable convergence behavior under grid refinement and produce approximate solutions that are comparable to those of classical numerical methods. We also exploited the linearity of the PDE to decompose the model problem into two subproblems. This decomposition improves both training efficiency and test accuracy. The decomposed formulations consistently outperform the original formulation, even when each decomposed formulation is trained with a substantially smaller number of training samples. Finally, we demonstrated the applicability of the proposed framework beyond Poisson equations through numerical experiments on the Helmholtz equation. These results indicate that the NICON framework is not limited to simple elliptic problems and can be extended to PDEs with oscillatory solutions. Future work may explore extensions to complex geometries, irregular boundaries, and new operator network architectures, as well as a broader class of PDEs.

## References

- [1] Yohai Bar-Sinai, Stephan Hoyer, Jason Hickey, and Michael P. Brenner, *Learning data-driven discretizations for partial differential equations*, Proceedings of the National Academy of Sciences **116** (2019), no. 31, 15344–15349.
- [2] Oussama Boussif, Yoshua Bengio, Loubna Benabbou, and Dan Assouline, *MAgNet: Mesh agnostic neural PDE solver*, Advances in Neural Information Processing Systems (Alice H. Oh, Alekh Agarwal, Danielle Belgrave, and Kyunghyun Cho, eds.), 2022.
- [3] Johannes Brandstetter, Daniel E. Worrall, and Max Welling, *Message passing neural PDE solvers*, International Conference on Learning Representations, 2022.
- [4] Shuhao Cao, *Choose a transformer: Fourier or Galerkin*, Advances in Neural Information Processing Systems (A. Beygelzimer, Y. Dauphin, P. Liang, and J. Wortman Vaughan, eds.), 2021.
- [5] Sung Woong Cho, Jae Yong Lee, and Hyung Ju Hwang, *Learning time-dependent PDE via graph neural networks and deep operator network for robust accuracy on irregular grids*, Journal of Computational Physics **544** (2026), 114430.
- [6] Woojin Cho, Minju Jo, Haksoo Lim, Kookjin Lee, Dongeun Lee, Sanghyun Hong, and Noseong Park, *Parameterized physics-informed neural networks for parameterized PDEs*, Proceedings of the 41st International Conference on Machine Learning (Ruslan Salakhutdinov, Zico Kolter, Katherine Heller, Adrian Weller, Nuria Oliver, Jonathan Scarlett, and Felix Berkenkamp, eds.), Proceedings of Machine Learning Research, vol. 235, PMLR, 21–27 Jul 2024, pp. 8510–8533.
- [7] Woojin Cho, Kookjin Lee, Donsub Rim, and Noseong Park, *Hypernetwork-based meta-learning for low-rank physics-informed neural networks*, Thirty-seventh Conference on Neural Information Processing Systems, 2023.
- [8] Maarten de Hoop, Daniel Huang, Elizabeth null, and Andrew Stuart, *The cost-accuracy trade-off in operator learning with neural networks*, Journal of Machine Learning **1** (2022), 299–341.
- [9] Somdatta Goswami, Aniruddha Bora, Yue Yu, and George Em Karniadakis, *Physics-informed deep neural operator networks*, pp. 219–254, Springer International Publishing, Cham, 2023.
- [10] Zhongkai Hao, Zhengyi Wang, Hang Su, Chengyang Ying, Yinpeng Dong, Songming Liu, Ze Cheng, Jian Song, and Jun Zhu, *GNOT: A general neural operator transformer for operator learning*, Proceedings of the 40th International Conference on Machine Learning (Andreas Krause, Emma Brunskill, Kyunghyun Cho, Barbara Engelhardt, Sivan Sabato, and Jonathan Scarlett, eds.), Proceedings of Machine Learning Research, vol. 202, PMLR, 23–29 Jul 2023, pp. 12556–12569.

- [11] Youngjoon Hong, Seungchan Ko, and Jaeyong Lee, *Error analysis for finite element operator learning methods for solving parametric second-order elliptic PDEs*, arXiv preprint arXiv:2404.17868 (2024).
- [12] George Em Karniadakis, Ioannis G Kevrekidis, Lu Lu, Paris Perdikaris, Sifan Wang, and Liu Yang, *Physics-informed machine learning*, *Nature Reviews Physics* **3** (2021), no. 6, 422–440.
- [13] Nikola Kovachki, Zongyi Li, Burigede Liu, Kamyar Azizzadenesheli, Kaushik Bhattacharya, Andrew Stuart, and Anima Anandkumar, *Neural operator: Learning maps between function spaces with applications to PDEs*, *Journal of Machine Learning Research* **24** (2023), no. 89, 1–97.
- [14] Nikola B Kovachki, Samuel Lanthaler, and Hrushikesh Mhaskar, *Data complexity estimates for operator learning*, arXiv preprint arXiv:2405.15992 (2024).
- [15] Jae Yong Lee, SungWoong CHO, and Hyung Ju Hwang, *HyperDeepONet: learning operator with complex target function space using the limited resources via hypernetwork*, The Eleventh International Conference on Learning Representations, 2023.
- [16] Jae Yong Lee, Seungchan Ko, and Youngjoon Hong, *Finite element operator network for solving elliptic-type parametric PDEs*, *SIAM J. Sci. Comput.* **47** (2025), no. 2, C501–C528. MR 4888707
- [17] Zongyi Li, Nikola Borislavov Kovachki, Kamyar Azizzadenesheli, Burigede liu, Kaushik Bhattacharya, Andrew Stuart, and Anima Anandkumar, *Fourier neural operator for parametric partial differential equations*, International Conference on Learning Representations, 2021.
- [18] Zongyi Li, Hongkai Zheng, Nikola Kovachki, David Jin, Haoxuan Chen, Burigede Liu, Kamyar Azizzadenesheli, and Anima Anandkumar, *Physics-informed neural operator for learning partial differential equations*, *ACM/IMS Journal of Data Science* **1** (2024), no. 3.
- [19] Lu Lu, Pengzhan Jin, Guofei Pang, Zhongqiang Zhang, and George Em Karniadakis, *Learning nonlinear operators via DeepONet based on the universal approximation theorem of operators*, *Nature Machine Intelligence* **3** (2021), no. 3, 218–229.
- [20] Lu Lu, Xuhui Meng, Shengze Cai, Zhiping Mao, Somdatta Goswami, Zhongqiang Zhang, and George Em Karniadakis, *A comprehensive and fair comparison of two neural operators (with practical extensions) based on fair data*, *Computer Methods in Applied Mechanics and Engineering* **393** (2022), 114778.
- [21] Levi D. McCleny and Ulisses M. Braga-Neto, *Self-adaptive physics-informed neural networks*, *Journal of Computational Physics* **474** (2023), 111722.
- [22] M. Raissi, P. Perdikaris, and G. E. Karniadakis, *Physics-informed neural networks: a deep learning framework for solving forward and inverse problems involving nonlinear partial differential equations*, *Journal of Computational Physics* **378** (2019), 686–707. MR 3881695
- [23] Bogdan Raonic, Roberto Molinaro, Tim De Ryck, Tobias Rohner, Francesca Bartolucci, Rima Alaifari, Siddhartha Mishra, and Emmanuel de Bezenac, *Convolutional neural operators for robust and accurate learning of PDEs*, Thirty-seventh Conference on Neural Information Processing Systems, 2023.
- [24] Olaf Ronneberger, Philipp Fischer, and Thomas Brox, *U-net: Convolutional networks for biomedical image segmentation*, International Conference on Medical image computing and computer-assisted intervention, Springer, 2015, pp. 234–241.
- [25] Natarajan Sukumar and Ankit Srivastava, *Exact imposition of boundary conditions with distance functions in physics-informed deep neural networks*, *Computer Methods in Applied Mechanics and Engineering* **389** (2022), 114333.

- [26] Haixin Wang, Jiaxin LI, Anubhav Dwivedi, Kentaro Hara, and Tailin Wu, *BENO: Boundary-embedded neural operators for elliptic PDEs*, The Twelfth International Conference on Learning Representations, 2024.
- [27] Sifan Wang, Jacob H Seidman, Shyam Sankaran, Hanwen Wang, George J. Pappas, and Paris Perdikaris, *CViT: Continuous vision transformer for operator learning*, The Thirteenth International Conference on Learning Representations, 2025.
- [28] Sifan Wang, Yujun Teng, and Paris Perdikaris, *Understanding and mitigating gradient flow pathologies in physics-informed neural networks*, SIAM Journal on Scientific Computing **43** (2021), no. 5, A3055–A3081.
- [29] Sifan Wang, Hanwen Wang, and Paris Perdikaris, *Learning the solution operator of parametric partial differential equations with physics-informed DeepONets*, Science advances **7** (2021), no. 40, eabi8605.
- [30] Yinhao Zhu and Nicholas Zabaras, *Bayesian deep convolutional encoder-decoder networks for surrogate modeling and uncertainty quantification*, Journal of Computational Physics **366** (2018), 415–447. MR 3800689
- [31] Yinhao Zhu, Nicholas Zabaras, Phaedon-Stelios Koutsourelakis, and Paris Perdikaris, *Physics-constrained deep learning for high-dimensional surrogate modeling and uncertainty quantification without labeled data*, Journal of Computational Physics **394** (2019), 56–81. MR 3957452